

ON DIFFERENTIABLE LOCAL BOUNDS PRESERVING STABILIZATION FOR EULER EQUATIONS

SANTIAGO BADIA^{1,2}, JESÚS BONILLA^{2,3}, SIBUSISO MABUZA⁴, AND JOHN N. SHADID^{5,6}

ABSTRACT. This work presents the design of nonlinear stabilization techniques for the finite element discretization of Euler equations in both steady and transient form. Implicit time integration is used in the case of the transient form. A differentiable local bounds preserving method has been developed, which combines a Rusanov artificial diffusion operator and a differentiable shock detector. Nonlinear stabilization schemes are usually stiff and highly nonlinear. This issue is mitigated by the differentiability properties of the proposed method. Moreover, in order to further improve the nonlinear convergence, we also propose a continuation method for a subset of the stabilization parameters. The resulting method has been successfully applied to steady and transient problems with complex shock patterns. Numerical experiments show that it is able to provide sharp and well resolved shocks. The importance of the differentiability is assessed by comparing the new scheme with its non-differentiable counterpart. Numerical experiments suggest that, for up to moderate nonlinear tolerances, the method exhibits improved robustness and nonlinear convergence behavior for steady problems. In the case of transient problem, we also observe a reduction in the computational cost.

Keywords: Shock capturing, Euler equations, Hyperbolic systems, Positivity preservation

CONTENTS

1. Introduction	2
2. Preliminaries	3
2.1. Continuous problem	3
2.2. Discretization	4
2.3. Stabilization properties	5
3. Nonlinear stabilization	7
3.1. Differentiability	9
4. Nonlinear solver	10
5. Numerical experiments	11
5.1. Convergence test	11
5.2. Reflected Shock	13
5.3. Sod's Shock Tube	14
5.4. Scramjet	17
6. Conclusions	20
Acknowledgments	21
References	22

¹ School of Mathematics, Monash University, Clayton, Victoria, 3800, Australia.

² Centre Internacional de Mètodes Numèrics en Enginyeria (CIMNE), Esteve Terradas 5, 08860 Castelldefels, Spain.

³ Universitat Politècnica de Catalunya, Jordi Girona 1-3, Edifici C1, 08034 Barcelona, Spain.

⁴ School of Mathematical and Statistical Sciences, Clemson University, O-110 Martin Hall, Clemson, SC 29634, USA.

⁵ Center for Computing Research, Sandia National Laboratories, PO Box 5800, Albuquerque NM 87123, USA.

⁶ Department of Mathematics and Statistics, University of New Mexico, MSC01 1115, Albuquerque, NM 87131, USA.

E-mails:

santiago.badia@monash.edu (SB), jbonilla@cimne.upc.edu (JB), smabuza@clemson.edu (SM), jnshadi@sandia.gov (JS) .

1. INTRODUCTION

The solution of many hyperbolic conservation laws satisfies a number of mathematical and physics constraints. These can include, for example, maximum principles, positivity and monotonicity preservation. A classical example are the Euler equations, where positivity must be preserved for the density, internal energy, and therefore also the pressure. In general, discretizations can yield non-physical solutions that violate these properties, leading to nonlinear instabilities. This is a well known issue. In the context of explicit finite volume schemes or discontinuous Galerkin (dG) finite element (FE) methods, several stabilized schemes have already been developed [10, 30, 40]. However, explicit time integrators need to resolve all time scales for stability reasons. For some multiple-time-scale problems, this can often imply very stringent stability conditions on the time-step size. If the fastest time scales are critical to the dynamics, and therefore of scientific or engineering interest, then explicit time integrators are well suited. On the contrary, implicit time integration is favored when the smallest time-scales are not relevant to the dynamics of interest. For example, the ability to integrate accurately and efficiently for longer time-scale simulations can be essential in some plasma physics applications [22]. Moreover, explicit schemes become inefficient for steady problems because one is forced to solve all the hydrodynamic evolution until the steady state is reached. Therefore, the design of implicit *stabilized* schemes that preserve the previously mentioned structure continues to be an important challenge.

In this work, we focus on implicit continuous Galerkin (cG) FE approximations of steady and transient shock hydrodynamics problems. It is well known that the Galerkin method (without any modification) is generally unstable for hyperbolic problems and yields solutions with spurious oscillations [25, 26]. Therefore, FE schemes are usually supplemented with additional artificial diffusion terms. Those terms are designed such that the resulting scheme satisfies the properties of the continuous problem. For example, positive density and internal energy or non-decreasing entropy. Developing a numerical scheme that preserves these properties is very challenging. This becomes especially complex for nonlinear hyperbolic systems. A number of methods that preserve the continuous problem properties have been proposed. In the explicit finite difference and finite volume methods contexts, schemes in [14, 19, 20] preserve these properties for Euler and the p-system. Recently, Guermond and Popov [16] have extended these methods to explicit cG FE schemes. Their result is applicable to any first order hyperbolic system with bounded wave propagation speed. In [17], Guermond et al. improved their previous scheme to recover second order convergence. Moreover, they generalized it to different discretization approaches. However, this scheme is limited to explicit time integration. More recently, Kuzmin [24] has extended this method to monolithic convex limiting, which allow the usage of implicit time integrators. An alternative is to impose conditions based on the diagonalization of the problem. Since it is a hyperbolic system, then there exists a set of *characteristic* variables for which the system can be locally diagonalized and written as a set of independent transport problems. At this point, one can use techniques developed for scalar problems. Hence, the stabilization methods are based on adapting the scalar techniques for characteristic variables to the system written in the original set of variables. Following this strategy, some progress has been recently made in stabilized FE schemes by making use of flux corrected transport (FCT) algorithms [27, 31, 33, 34]. The schemes proposed therein are based on two main ingredients. On the one hand, a diffusive term able to minimize or eliminate any oscillatory behavior. On the other hand, a limiter, or shock detector, to modulate the stabilization term and restrict its action to the vicinity of shocks.

With this work focusing on steady and transient Euler equations, with implicit time-stepping in the transient case, our scheme is fully implicit. The nonlinearity of the Euler equations results in large nonlinear system of equations requiring a robust nonlinear solver. We will present and study a nonlinear solver by looking at its nonlinear convergence in addition to some standard validation. It is known that for certain limiter choices the convergence of the nonlinear solver might be remarkably hard [23]. Recent progress has been made to improve the convergence of the nonlinear solver for scalar convection-diffusion problems [2, 3, 7]. In these studies, the authors were able to improve the nonlinear convergence by proposing differentiable stabilization terms to improve convergence rates of the Newton iterative nonlinear solver. In this work, we extend the differentiable nonlinear stabilization in [2] to the

Euler equations using the ideas from [27, 34] to define the artificial diffusion operators for hyperbolic systems. The new method is applied to the steady and transient Euler equations, and its nonlinear convergence is assessed. The method proposed in the present work has been implemented and tested using the FEMPAR library [4, 5].

The paper is structured as follows. In Sect. 2 we present the CG discretization for Euler equations. Sect. 3 is devoted to the definition of the stabilization terms. We describe the nonlinear solvers used in Sect. 4. Then, in Sect. 5 we present the numerical experiments performed. Finally, we draw some conclusions in Sect. 6.

2. PRELIMINARIES

In this section, we introduce the continuous problem and its FE discretization. At the end of the section, the basic ingredients for desired stabilized schemes for hyperbolic systems are presented.

2.1. Continuous problem. Consider an open, bounded, and connected domain, $\Omega \subset \mathbb{R}^d$, where d is the number of spatial dimensions. Let $\partial\Omega$ be the Lipschitz continuous boundary of Ω . A first order hyperbolic problem can be written in conservative form as

$$\begin{cases} \partial_t \mathbf{u} + \nabla \cdot \mathbf{f}(\mathbf{u}) = \mathbf{g}, & \text{in } \Omega \times (0, T], \\ \mathbf{u}(x, 0) = \mathbf{u}_0(x), & x \in \Omega, \end{cases} \quad (1)$$

where $\mathbf{u} = \{u^\beta\}_{\beta=1}^m$ are $m \geq 1$ conserved variables, \mathbf{f} is the physical flux, \mathbf{u}_0 are the given initial conditions, and $\mathbf{g}(x, t)$ is a function defining the body forces. Note that the flux, $\mathbf{f} : \mathbb{R}^m \rightarrow \mathbb{R}^{m \times d}$, has components $\mathbf{f} = \{\mathbf{f}_i\}_{i=1}^d$, where $\mathbf{f}_i : \mathbb{R}^m \rightarrow \mathbb{R}^m$ is the flux in the i th spatial direction. Note that if $m = 1$, and $\mathbf{f}(u) \doteq \mathbf{v}(x, t)u$ with $\mathbf{v}(x, t)$ a divergence-free convection field, we recover the well known linear scalar convection problem. For Euler equations we have $m = d + 2$ and

$$\mathbf{u} \doteq \begin{pmatrix} \rho \\ \mathbf{m} \\ \rho E \end{pmatrix}, \quad \mathbf{f} \doteq \begin{pmatrix} \mathbf{m} \\ \mathbf{m} \otimes \mathbf{v} + p\mathbb{I} \\ \mathbf{v}(\rho E + p) \end{pmatrix}, \quad \text{and} \quad \mathbf{g} \doteq \begin{pmatrix} 0 \\ \mathbf{b} \\ \mathbf{b} \cdot \mathbf{v} + r \end{pmatrix},$$

where ρ is the density, ρE is the total energy, p is the pressure, $\mathbf{m} = \{m_1, \dots, m_d\}$, where $m_i = \rho v_i$, is the momentum, $\mathbf{v} = \{v_1, \dots, v_d\}$ is the velocity, $\mathbf{b} = \{b_1, \dots, b_d\}$ are the body forces, r is an energy source term per unit mass, and \mathbb{I} an identity matrix of dimension d . In addition, the system is equipped with the ideal gas equation of state $p = (\gamma - 1)\rho e$, where $\rho e = \rho E - \frac{1}{2}\rho\|\mathbf{v}\|^2$ is the internal energy, and γ is the adiabatic index. We will also consider the steady counterpart of (1), which is obtained by dropping the time derivative term and the initial conditions.

Boundary conditions for this system may be imposed strongly or numerically, see [12, 18, 40] for details. Here we will present one approach that makes use of the eigensystem of the Euler equations to define inlet and outlet boundaries. Denote by $\mathbf{f}' : \mathbb{R}^m \rightarrow \mathbb{R}^{m \times m \times d}$ the flux Jacobian. Let $\mathbf{n} \in \mathbb{R}^d$ be any direction vector. Since the system is hyperbolic the flux Jacobian in any direction is diagonalizable and has only real eigenvalues, i.e. $\mathbf{f}'(\mathbf{u}) \cdot \mathbf{n} = \sum_{i=1}^d \mathbf{f}'_i(\mathbf{u})n_i$ is diagonalizable with real eigenvalues, say $\{\lambda_\beta\}_{\beta=1}^m$. These eigenvalues might have different multiplicities, and different signs. Hence, for a given direction, \mathbf{n} , each characteristic variable might be convected forward (along \mathbf{n}) or backwards (along $-\mathbf{n}$). Therefore, it is convenient to define inflow and outflow boundaries for each component. The inflow boundary for component β is defined as $\Gamma_{\text{in}}^\beta \doteq \{\mathbf{x} \in \partial\Omega : \lambda_\beta(\mathbf{f}'(\mathbf{u}) \cdot \mathbf{n}_{\partial\Omega}) \leq 0\}$, where $\mathbf{n}_{\partial\Omega}$ is the unit outward normal to the boundary, and λ_β is the β th-eigenvalue of the flux Jacobian. We define the outflow boundary as $\Gamma_{\text{out}}^\beta \doteq \partial\Omega \setminus \Gamma_{\text{in}}^\beta$. From this, we can define some inflow boundary conditions as follows

$$u^\beta(x, t) = \bar{u}^\beta(x, t), \quad \text{on } \Gamma_{\text{in}}^\beta \times (0, T], \quad \beta = 1, \dots, m,$$

where $\bar{u}^\beta(x, t)$ are the boundary values for the β th-component of \mathbf{u} .

2.2. Discretization. Let \mathcal{T}_h be a conforming partition of Ω . The set of nodes of the mesh \mathcal{T}_h is denoted by \mathcal{N}_h . For every node $i \in \mathcal{N}_h$, the nodal coordinates are given by \mathbf{x}_i . We denote by $N = \text{card}(\mathcal{N}_h)$ the total number of nodes. The set of nodes belonging to a particular element $K \in \mathcal{T}_h$ is denoted by $\mathcal{N}_h(K) \doteq \{i \in \mathcal{N}_h : \mathbf{x}_i \in K\}$. Moreover, Ω_i is the macroelement made up of elements that contain node i , i.e., $\Omega_i \doteq \bigcup_{K \in \mathcal{T}_h, \mathbf{x}_i \in K} K$. To simplify the discussion below, we use i for both the node and its associated index.

We will make use of linear/bilinear finite elements. Define $\mathbf{V}_h = (V_h)^m$, where for simplex meshes, $V_h \doteq \{v_h \in \mathcal{C}^0(\Omega) : v_h|_K \in \mathcal{P}_1(K) \forall K \in \mathcal{T}_h\}$, where m is the number of components of \mathbf{u} , and $\mathcal{P}_1(\Omega)$ is the space of polynomials of total degree less than or equal to one. For d -cube partitions, $V_h \doteq \{v_h \in \mathcal{C}^0(\Omega) : v_h|_K \in Q_1(K), \forall K \in \mathcal{T}_h\}$, where $Q_1(K)$ is space of polynomials of partial degree less than or equal to one. Any function $\mathbf{v}_h \in \mathbf{V}_h$ is a linear combination of the basis $\{\varphi_i\}_{i \in \mathcal{N}_h}$ with nodal values \mathbf{v}_i , where φ_i is the shape function associated to the node i . Hence, $\mathbf{v}_h = \sum_{i \in \mathcal{N}_h} \varphi_i \mathbf{v}_i$.

We use standard notation for Lebesgue spaces. The $L^2(\omega)$ scalar product is denoted by $(\cdot, \cdot)_\omega$ for any set ω . However, we omit the subscript for $\omega \equiv \Omega$. The L^2 norm is denoted by $\|\cdot\|$.

The scheme will be based on the method of lines. First, we present the spatial discretization. The solution is approximated in space using the FE spaces defined above, i.e., $\mathbf{u} \approx \mathbf{u}_h = \sum_{i \in \mathcal{N}_h} \varphi_i \mathbf{u}_i$. In addition, we use the group-FEM technique to approximate the fluxes [6, 13, 27, 34]. Thus, the fluxes are approximated as follows $\mathbf{f}(\mathbf{u}_h) \approx \mathbf{f}_h(\mathbf{u}_h) := \sum_{i \in \mathcal{N}_h} \varphi_i \mathbf{f}(\mathbf{u}_i)$. To get the semi-discrete scheme, we test the strong form against $\mathbf{v}_h \in \mathbf{V}_h$. Afterwards, we apply integration by parts in the convective term. Therefore, the semi-discrete problem is given as follows: find $\mathbf{u}_h \in \mathbf{V}_h$, with $\mathbf{u}_h = \mathbf{u}_{0h}$ at $t = 0$, such that

$$(\partial_t \mathbf{u}_h, \mathbf{v}_h) - (\mathbf{f}_h(\mathbf{u}_h), \nabla \mathbf{v}_h) + (\mathbf{n}_{\partial\Omega} \cdot \mathbf{f}_h(\mathbf{u}_h), \mathbf{v}_h)_{\partial\Omega} = (\mathbf{g}, \mathbf{v}_h), \text{ for all } \mathbf{v}_h \in \mathbf{V}_h,$$

where \mathbf{u}_{0h} is an LED projection of \mathbf{u}_0 onto \mathbf{V}_h [27]. Note that for the sake of simplicity boundary conditions are strongly imposed on the conserved variables. This procedure implies that the number of unknowns in the discrete system is reduced after prescribing boundary conditions. Therefore, the equations corresponding to prescribed values are also removed from the algebraic system. This practice is suitable only for simple problems. Transonic flow and other complex problems may require fairly complex boundary conditions. These may include numerical flux boundary conditions [18].

For the time discretization, we only consider the Backward Euler (BE) scheme. Other time integrators may be considered, such as the strong stability preserving (SSP) Runge Kutta (RK) methods (see [15]). We will now discretize the semi-discrete scheme in time to get fully discrete scheme. Consider a partition of the time domain $(0, T]$ into n^{ts} sub-intervals of length $\Delta t_{n+1} = t^{n+1} - t^n$. Then, at every time step $n = 0, \dots, n^{ts} - 1$, the fully discrete scheme is

$$\mathbf{M} \delta_t \mathbf{U}^{n+1} + \mathbf{K}(\mathbf{u}_h^{n+1}) \mathbf{U}^{n+1} = \mathbf{G},$$

where $\mathbf{U}^{n+1} \doteq [\mathbf{u}_1^{n+1}, \dots, \mathbf{u}_N^{n+1}]^T$ is the vector of nodal values at time t^{n+1} , and $\delta_t(\mathbf{U}) \doteq \Delta t_{n+1}^{-1}(\mathbf{U}^{n+1} - \mathbf{U}^n)$. \mathbf{M} and \mathbf{K} are block matrices. \mathbf{G} is a block vector. They are given by

$$\begin{aligned} \mathbf{M} &= \{\mathbf{M}_{ij}\}_{i,j=1}^N, \\ \mathbf{K} &= \{\mathbf{K}_{ij}\}_{i,j=1}^N, \\ \mathbf{G} &= \{\mathbf{G}_i\}_{i=1}^N. \end{aligned}$$

Each \mathbf{M}_{ij} is an $m \times m$ matrix. So is \mathbf{K}_{ij} . \mathbf{G}_i is an $m \times 1$ vector. These block matrix and vector entries are given for any $i, j \in \mathcal{N}_h$ by

$$\begin{aligned} \mathbf{M}_{ij} &= \{\mathbf{M}_{ij}^{\beta\gamma}\}_{\beta,\gamma=1}^m, & \mathbf{M}_{ij}^{\beta\gamma} &\doteq (\varphi_j, \varphi_i) \delta_{\beta\gamma}, \\ \mathbf{K}_{ij} &= \{\mathbf{K}_{ij}^{\beta\gamma}\}_{\beta,\gamma=1}^m, & \mathbf{K}_{ij}^{\beta\gamma} &\doteq -(\varphi_j \delta_{\beta\xi}, \mathbf{f}'_k(\mathbf{u}_j^{n+1})^{\xi\eta} \cdot \partial_k \varphi_i \delta_{\eta\gamma}) + (\varphi_j \delta_{\beta\xi}, n_k \cdot \mathbf{f}'_k(\mathbf{u}_j^{n+1})^{\xi\eta} \varphi_i \delta_{\eta\gamma})_{\partial\Omega}, \\ \mathbf{G}_i &= \{\mathbf{G}_i^\beta\}_{\beta=1}^m, & \mathbf{G}_i^\beta &\doteq (\mathbf{g}^\beta, \varphi_i), \end{aligned}$$

where Einstein summation applies over k, ξ and η . $\beta, \gamma, \xi, \eta \in \{1, \dots, m\}$ are the component indices,

and $\delta_{\beta\gamma}$ is the Kronecker delta. Notice that we have rearranged the terms in $\mathbf{K}_{ij}^{\beta\gamma}$ using the fact that the Euler flux is homogeneous of degree one, i.e., $\mathbf{f}(\mathbf{u}_i) = \mathbf{f}'(\mathbf{u}_i)\mathbf{u}_i$.

2.3. Stabilization properties. In this section, we introduce some concepts required for discussing the stabilization presented in section 3. Stabilization for hyperbolic systems is developed from techniques designed for scalar equations. We briefly review below the ideas that govern stabilization for scalar problems.

Definition 2.1 (Local Discrete Extremum). *The function $v_h \in V_h$ has a local discrete minimum (resp. maximum) on $i \in \mathcal{N}_h$ if $u_i \leq u_j$ (resp. $u_i \geq u_j$) $\forall j \in \mathcal{N}_h(\Omega_i)$.*

Definition 2.2 (Local discrete maximum principle (DMP)). *A solution $u_h \in V_h$ satisfies the local discrete maximum principle if for every $i \in \mathcal{N}_h$*

$$\min_{j \in \mathcal{N}_h(\Omega_i) \setminus \{i\}} u_j \leq u_i \leq \max_{j \in \mathcal{N}_h(\Omega_i) \setminus \{i\}} u_j.$$

Definition 2.3 (LED). *A scheme is local extremum diminishing if, for every u_i that is a local discrete maximum (resp. minimum),*

$$\frac{du_i}{dt} \leq 0, \quad \left(\text{resp. } \frac{du_i}{dt} \geq 0 \right),$$

is satisfied.

Given a scalar problem with the forcing term $\mathbf{g} \equiv 0$, a semi-discrete scheme may be written as

$$\sum_j (\mathbf{M}_{ij} \frac{du_j}{dt} + \mathbf{A}_{ij} u_j) = 0,$$

plus appropriate boundary conditions. One possible strategy for satisfying the above properties consists of designing a scheme that yields a positive diagonal mass matrix $\mathbf{M}_{ij} = m_i \delta_{ij}$, where $m_i > 0$, and a matrix \mathbf{A} that satisfies

$$\sum_j \mathbf{A}_{ij} = 0, \quad \text{and} \quad \mathbf{A}_{ij} \leq 0, \quad i \neq j. \quad (2)$$

In this case, it is possible to rewrite the system as

$$m_i \frac{du_i}{dt} + \sum_{j \in \mathcal{N}_h(\Omega_i) \setminus \{i\}} \mathbf{A}_{ij} (u_j - u_i) = 0, \quad \forall i \in \mathcal{N}_h. \quad (3)$$

As shown in [11] and [29], such a scheme satisfies the local DMP for steady problems and it is also local extremum diminishing (LED) when applied to transient problems.

The extension of these properties to hyperbolic systems is based on analyzing them in characteristic variables. Let us consider a one-dimensional linear hyperbolic system with a constant Jacobian flux, \mathbf{f}' . In this particular case, the continuous system can be diagonalized. Thus it is possible to discretize and solve for the characteristic variables. For example, for the set of characteristic variables, say W , the continuous system reads:

$$\partial_t W + \Lambda \partial_x W = 0, \quad (4)$$

where $\Lambda = \text{diag}(\lambda_1, \dots, \lambda_m)$ is a diagonal m by m matrix. At this point, one can see the system as a set of independent scalar transport problems. Thus, it leads to a system with diagonal blocks after discretizing it with FEs.

Assuming conditions (2) are satisfied for every component of problem (4), then the scheme will be LED for each characteristic variable. Notice that this is equivalent to forcing the original (coupled) FE approximation to have negative semi-definite off-diagonal blocks. That is, the FE discretization of the problem in characteristic variables reads

$$(\varphi_j, \varphi_i) \partial_t W_j + \Lambda (\partial_x \varphi_j, \varphi_i) W_j = 0. \quad (5)$$

Since in this case it is a one dimensional linear problem, we can recover the original problem using the fact that $W = R^{-1}U$, and $\mathbf{f}' = R\Lambda R^{-1}$. Multiplying (5) at the left by R ,

$$(\varphi_j, \varphi_i) \partial_t \bar{R} R^{-1} U_j + R \Lambda (\partial_x \varphi_j, \varphi_i) R^{-1} U_j = 0.$$

In this case, $(\partial_x \varphi_j, \varphi_i)$ is simply a scalar value. Hence, we are able to recover the original (coupled) problem FE discretization.

$$(\varphi_j, \varphi_i) \partial_t U_j + \mathbf{f}'(\partial_x \varphi_j, \varphi_i) U_j = 0.$$

Thus, if $\mathbf{f}'(\partial_x \varphi_j, \varphi_i)$ is negative semi-definite for $j \neq i$, then the problem in characteristic variables will satisfy conditions (2) for each variable.

In the case of more general multidimensional problems (e.g. Euler equations), this would *only* imply that the scheme is LED for a certain set of *local* characteristic variables. Furthermore, if the flux Jacobian \mathbf{f}' is not linear, then even the definition of the matrix \mathbf{A}_{ij} (relating nodes i and j) is not trivial. Let us recall the definition of these blocks for Euler equations

$$\mathbf{K}_{ij} \doteq -(\varphi_j, \mathbf{f}'_k(\mathbf{u}_j) \cdot \partial_k \varphi_i) + (\varphi_j, n_k \cdot \mathbf{f}'_k(\mathbf{u}_j) \varphi_i) \partial \Omega = \mathbf{f}'_k(\mathbf{u}_j) \cdot (\partial_k \varphi_j, \varphi_i),$$

where we have undone integration by parts. It is easy to check that $\sum_j (\partial_k \varphi_j, \varphi_i) = 0$. Hence, we can write

$$\sum_{j \in \mathcal{N}_h(\Omega_i)} \mathbf{K}_{ij} \mathbf{u}_j = \sum_{j \in \mathcal{N}_h(\Omega_i) \setminus \{i\}} (\partial_k \varphi_j, \varphi_i) (\mathbf{f}'_k(\mathbf{u}_j) \cdot \mathbf{u}_j - \mathbf{f}'_k(\mathbf{u}_i) \cdot \mathbf{u}_i).$$

As previously stated, it is not straightforward in the case of Euler equations to rewrite the discrete problem in the form of (3). However, making use of special density-averaged variables it is possible to rewrite the previous expression as

$$\sum_{j \in \mathcal{N}_h(\Omega_i)} \mathbf{K}_{ij} \mathbf{u}_j = \sum_{j \in \mathcal{N}_h(\Omega_i) \setminus \{i\}} \mathbf{f}'_k(\mathbf{u}_{ij}) \cdot (\partial_k \varphi_j, \varphi_i) (\mathbf{u}_j - \mathbf{u}_i),$$

where \mathbf{u}_{ij} are the Roe mean values [35]. For an ideal gas, these are defined as

$$\rho_{ij} = \sqrt{\rho_i \rho_j}, \quad \mathbf{m}_{ij} = \frac{\mathbf{m}_i \sqrt{\rho_j} + \mathbf{m}_j \sqrt{\rho_i}}{\sqrt{\rho_i} + \sqrt{\rho_j}}, \quad (\rho E)_{ij} = \frac{1}{\gamma} \left(\rho_{ij} H_{ij} + (\gamma - 1) \frac{|\mathbf{m}_{ij}|^2}{2\rho_{ij}} \right),$$

where H_{ij} is the average enthalpy

$$H_{ij} = \frac{H_i \sqrt{\rho_i} + H_j \sqrt{\rho_j}}{\sqrt{\rho_i} + \sqrt{\rho_j}}, \quad \text{and} \quad H_i = \frac{\rho E_i + p_i}{\rho_i}.$$

Therefore, using this density-averaged variables it is possible to rewrite Euler problem in the form of (3). Hence, if $-\mathbf{f}'_k(\mathbf{u}_{ij}) \cdot (\partial_k \varphi_j, \varphi_i)$ has non-positive eigenvalues, then the scheme will be LED for a certain set of *local* characteristic variables. Schemes that satisfy this property are named *local bounds preserving schemes* in the literature [34]. This reasoning above motivated the definition of the LED *principle* for hyperbolic systems of equations by Kuzmin [25] and coworkers. Adapted from this principle, we define local bounds preserving schemes as follows.

Definition 2.4. *The semi-discrete scheme*

$$m_i \partial_t \mathbf{u}_i + \sum_{j \neq i} \mathbf{A}_{ij} (\mathbf{u}_j - \mathbf{u}_i) = \mathbf{0}$$

is said to be local bounds preserving if \mathbf{M} is diagonal with positive entries (i.e. $\mathbf{M}_{ij} = m_i \delta_{ij} I_{m \times m}$), \mathbf{A}_{ij} has non-positive eigenvalues for every $j \neq i$, and $\sum_j \mathbf{A}_{ij} = \mathbf{0}$.

Unfortunately, to the best of our knowledge, satisfying this definition does not guarantee positivity for density or internal energy. It also does not guarantee non-decreasing entropy. In any case, numerical schemes based on this definition have shown good numerical behavior [25, 28, 31, 34]. In the stabilization presented in these papers, conservative artificial diffusion is used. There are different types of artificial diffusion. The simplest is scalar artificial diffusion which is based on the spectral radius of \mathbf{A}_{ij} [25, 32]. This diffusion is also called Rusanov artificial diffusion, since for linear FEs or finite volume methods in one dimension, the scheme is equivalent to the Rusanov approximate Riemann

solver [25, 40]. Without any special treatment, adding artificial diffusion results in a first order accurate scheme. The key to recovering high-order convergence is to modulate the action of the artificial diffusion term, and restrict its action to the vicinity of discontinuities. Here, we construct a stabilization term using Rusanov artificial diffusion and a differentiable shock detector recently developed for scalar problems [2, 7]. This will be discussed extensively in the next section.

3. NONLINEAR STABILIZATION

In the previous section, we mentioned that the Galerkin FE discretization yields oscillatory solutions in regions around discontinuities. We supplement the original scheme with an artificial diffusion term to stabilize it and mitigate these oscillations. The proposed stabilization term is given by

$$B_h(\mathbf{u}_h; \mathbf{u}_h, \mathbf{v}_h) \doteq \sum_{K_e \in \mathcal{T}_h} \sum_{i,j \in \mathcal{N}_h(K_e)} \nu_{ij}^e(\mathbf{w}_h) \ell(i,j) \mathbf{v}_i \cdot I_{m \times m} \mathbf{u}_j, \quad (6)$$

for any $\mathbf{u}_h \in \mathbf{V}_h$ and $\mathbf{v}_h \in \mathbf{V}_h$. Here, $\ell(i,j) \doteq 2\delta_{ij} - 1$ is a graph Laplacian operator defined in [2], and $\nu_{ij}^e(\mathbf{w}_h)$ is the element-wise artificial diffusion defined as

$$\begin{aligned} \nu_{ij}^e(\mathbf{w}_h) &\doteq \max(\boldsymbol{\alpha}_i(\mathbf{w}_h) \lambda_{ij}^{\max}, \boldsymbol{\alpha}_j(\mathbf{w}_h) \lambda_{ji}^{\max}), \quad \text{for } j \in \mathcal{N}_h(\Omega_i) \setminus \{i\}, \\ \nu_{ii}^e(\mathbf{w}_h) &\doteq \sum_{j \in \mathcal{N}_h(\Omega_i) \setminus \{i\}} \nu_{ij}^e(\mathbf{w}_h), \end{aligned} \quad (7)$$

where λ_{ij}^{\max} is the spectral radius of the elemental convection matrix relating nodes $i, j \in \mathcal{N}_h$. We will also denote the spectral radius by $\kappa(\cdot)$, i.e., $\kappa(\mathbf{f}'(\mathbf{u}_{ij}) \cdot (\nabla \varphi_j, \varphi_i)_{K_e})$. As previously introduced, this artificial diffusion term is based on Rusanov scalar diffusion [27]. It is important to mention that the eigenvalues of these matrices can be easily computed as

$$\lambda_{1,\dots,d} = \mathbf{v}_{ij} \cdot \mathbf{c}_{ij}^e, \quad \lambda_{d+1} = \mathbf{v}_{ij} \cdot \mathbf{c}_{ij}^e - c \|\mathbf{c}_{ij}^e\|, \quad \lambda_{d+2} = \mathbf{v}_{ij} \cdot \mathbf{c}_{ij}^e + c \|\mathbf{c}_{ij}^e\| \quad (8)$$

where

$$\mathbf{c}_{ij}^e = (\nabla \varphi_j, \varphi_i)_{K_e}, \quad \text{and} \quad c = \sqrt{(\gamma - 1) \left(H_{ij} - \frac{|\mathbf{m}_{ij}|^2}{2\rho_{ij}^2} \right)}.$$

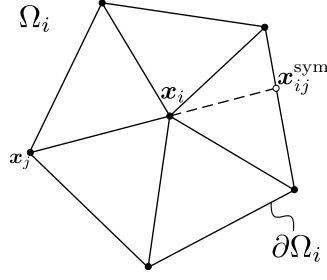
We denote by $\boldsymbol{\alpha}_i(\mathbf{w}_h)$ the shock detector used for modulating the action of the artificial diffusion term. The idea behind the definition of this detector is minimizing the amount of artificial diffusion introduced while stabilizing any oscillatory behavior. In regions where the local DMP (see Def. 2.2) is not satisfied for any chosen set of components, we ensure that Def. 2.4 is satisfied. $\boldsymbol{\alpha}_i(\mathbf{w}_h)$ must be a positive real number which takes value 1 when $u_h(\mathbf{x}_i)$ is an inadmissible value of \mathbf{u}_h , and smaller than 1 otherwise. To this end, we define

$$\boldsymbol{\alpha}_i(\mathbf{u}_h) \doteq \max\{\alpha_i(u_h^\beta)\}_{\beta \in C}, \quad (9)$$

where C is the set of components that are used to detect inadmissible values of \mathbf{u}_h , e.g. density and total energy in the case of Euler equations. For simplicity, we restrict ourselves to the components of \mathbf{u}_h . However, derived quantities such as the pressure or internal energy can be also used.

In order to introduce the shock detector, let us recall some useful notation from [2]. Let $\mathbf{r}_{ij} = \mathbf{x}_j - \mathbf{x}_i$ be the vector pointing from node \mathbf{x}_i to \mathbf{x}_j with $i, j \in \mathcal{N}_h$ and $\hat{\mathbf{r}}_{ij} \doteq \frac{\mathbf{r}_{ij}}{|\mathbf{r}_{ij}|}$. Recall that the set of points \mathbf{x}_j for $j \in \mathcal{N}_h(\Omega_i) \setminus \{i\}$ define the macroelement Ω_i around node \mathbf{x}_i . Let $\mathbf{x}_{ij}^{\text{sym}}$ be the point at the intersection between $\partial\Omega_i$ and the line that passes through \mathbf{x}_i and \mathbf{x}_j that is not \mathbf{x}_j (see Fig. 1). The set of all $\mathbf{x}_{ij}^{\text{sym}}$ for all $j \in \mathcal{N}_h(\Omega_i) \setminus \{i\}$ is represented with $\mathcal{N}_h^{i,\text{sym}}$. We define $\mathbf{r}_{ij}^{\text{sym}} \doteq \mathbf{x}_{ij}^{\text{sym}} - \mathbf{x}_i$. Given $\mathbf{x}_{ij}^{\text{sym}}$ in two dimensions, let us call a and b the indices of the vertices such that they define the edge in $\partial\Omega_i$ that contains $\mathbf{x}_{ij}^{\text{sym}}$. We define $\mathbf{u}_j^{\text{sym}}$ as the value of \mathbf{u}_h at $\mathbf{x}_{ij}^{\text{sym}}$, i.e. $\mathbf{u}_h(\mathbf{x}_{ij}^{\text{sym}})$.

Both $\mathbf{u}_{ij}^{\text{sym}}$ and $\mathbf{x}_{ij}^{\text{sym}}$ are only required to construct a linearity preserving shock detector. Let us define the jump and the mean of a linear approximation of component β of the unknown gradient at

FIGURE 1. u^{sym} drawing

node \mathbf{x}_i in direction \mathbf{r}_{ij} as

$$\begin{aligned} \llbracket \nabla u_h^\beta \rrbracket_{ij} &\doteq \frac{u_j^\beta - u_i^\beta}{|\mathbf{r}_{ij}|} + \frac{u_j^{\text{sym},\beta} - u_i^\beta}{|\mathbf{r}_{ij}^{\text{sym}}|}, \\ \left\{ \left| \nabla u_h^\beta \cdot \hat{\mathbf{r}}_{ij} \right| \right\}_{ij} &\doteq \frac{1}{2} \left(\frac{|u_j^\beta - u_i^\beta|}{|\mathbf{r}_{ij}|} + \frac{|u_j^{\text{sym},\beta} - u_i^\beta|}{|\mathbf{r}_{ij}^{\text{sym}}|} \right). \end{aligned}$$

In the present work, for each component in C , we use the same shock detector developed in [2]. Let us recall its definition

$$\alpha_i(u_h^\beta) \doteq \begin{cases} \left[\frac{\left| \sum_{j \in \mathcal{N}_h(\Omega_i)} \llbracket \nabla u_h^\beta \rrbracket_{ij} \right|}{\sum_{j \in \mathcal{N}_h(\Omega_i)} 2 \left\{ \left| \nabla u_h^\beta \cdot \hat{\mathbf{r}}_{ij} \right| \right\}_{ij}} \right]^q & \text{if } \sum_{j \in \mathcal{N}_h(\Omega_i)} \left\{ \left| \nabla u_h^\beta \cdot \hat{\mathbf{r}}_{ij} \right| \right\}_{ij} \neq 0 \\ 0 & \text{otherwise} \end{cases} \quad (10)$$

From [2, Lm. 3.1] we know that (10) is valued between 0 and 1, and it is only equal to one if $u_h^\beta(\mathbf{x}_i)$ is a local discrete extremum (in a space-time sense as in Def. 2.1). Since the linear approximations of the unknown gradients are exact for $u_h^\beta \in \mathcal{P}_1$, the shock detector vanishes when the solution is linear. Thus, it is also linearly preserving for every component in C . This result follows directly from [2, Th. 4.5].

The final stabilized problem in matrix form reads as follows. Find $\mathbf{u}_h \in \mathbf{V}_h$ such that $u_h^\beta = \bar{u}_h^\beta$ on Γ_{in}^β , $\mathbf{u}_h = \mathbf{u}_{0h}$ at $t = 0$, and

$$\bar{\mathbf{M}}(\mathbf{u}_h^{n+1}) \delta_t \mathbf{U}^{n+1} + \bar{\mathbf{K}}(\mathbf{u}_h^{n+1}) \mathbf{U}^{n+1} = \mathbf{G} \quad (11)$$

for $n = 1, \dots, n^{\text{ts}}$, where

$$\bar{\mathbf{M}}_{ij}(\mathbf{u}_h^{n+1}) \doteq [1 - \max(\alpha_i, \alpha_j)] (\varphi_j, \varphi_i) I_{m \times m} + \max(\alpha_i, \alpha_j) (\delta_{ij}, \varphi_i) I_{m \times m},$$

$$\bar{\mathbf{K}}_{ij}(\mathbf{u}_h^{n+1}) \doteq \mathbf{K}_{ij} + \mathbf{B}_{ij}, \text{ and } \mathbf{B}_{ij}(\mathbf{u}_h) \doteq \sum_{K_e \in \mathcal{T}_h} \nu_{ij}^e(\mathbf{u}_h) \ell(i, j) I_{m \times m}.$$

Lemma 3.1 (Local bounds preservation). *Consider $\mathbf{u}_h \in \mathbf{V}_h$ with component β in the set of tracked variables C . The stabilized problem (11), with $\mathbf{G} = \mathbf{0}$, is local bounds preserving as defined in Def. 2.4 at any region where u_h^β has extreme values.*

Proof. If component $\beta \in C$ of \mathbf{u}_h has an extremum at \mathbf{x}_i , then from [2, Lm. 3.1] we know that $\alpha_i(u_h^\beta) = 1$. Moreover, from (9) is easy to see that $\alpha_i(\mathbf{u}_h) = 1$. In this case, $\bar{\mathbf{M}}_{ij}(\mathbf{u}_h) = (\delta_{ij}, \varphi_i) I_{m \times m}$. Hence, $\bar{\mathbf{M}}_{ij}(\mathbf{u}_h) = 0$ for $j \neq i$ and $\bar{\mathbf{M}}_{ii}(\mathbf{u}_h) = m_i$. Therefore, we can rewrite the system as follows

$$\begin{aligned} m_i \partial_t \mathbf{u}_i + \sum_{j \in \mathcal{N}_h(\Omega_i) \setminus \{i\}} \bar{\mathbf{K}}_{ij}(\mathbf{u}_{ij}) (\mathbf{u}_j - \mathbf{u}_i) = \\ m_i \partial_t \mathbf{u}_i + \sum_{j \in \mathcal{N}_h(\Omega_i) \setminus \{i\}} \sum_{K_e \in \mathcal{T}_h} (\mathbf{f}'(\mathbf{u}_{ij}) \cdot (\nabla \varphi_j, \varphi_i)_{K_e} - \nu_{ij}^e I_{m \times m}) (\mathbf{u}_j - \mathbf{u}_i) = \mathbf{0}. \end{aligned}$$

We need to prove that the eigenvalues of $\bar{\mathbf{K}}_{ij}(\mathbf{u}_{ij})$ are non-positive. To this end, let us show the following inequality holds

$$\sum_{K_e \in \mathcal{T}_h} \kappa(\mathbf{f}'(\mathbf{u}_{ij}) \cdot (\nabla \varphi_j, \varphi_i)_{K_e}) \geq \kappa(\mathbf{f}'(\mathbf{u}_{ij}) \cdot (\nabla \varphi_j, \varphi_i)).$$

From (8), it is easy to check that $\kappa(\mathbf{f}'(\mathbf{u}_{ij}) \cdot (\nabla \varphi_j, \varphi_i)_{K_e}) = |\mathbf{v}_{ij} \cdot \mathbf{c}_{ij}^e| + c \|\mathbf{c}_{ij}^e\|$. Since $\mathbf{c}_{ij} = \sum_{K_e \in \mathcal{T}_h} \mathbf{c}_{ij}^e$, we have that

$$\sum_{K_e \in \mathcal{T}_h} |\mathbf{v}_{ij} \cdot \mathbf{c}_{ij}^e| \geq |\mathbf{v}_{ij} \cdot \mathbf{c}_{ij}|, \quad \text{and} \quad \sum_{K_e \in \mathcal{T}_h} c \|\mathbf{c}_{ij}^e\| \geq c \|\mathbf{c}_{ij}\|.$$

Therefore, $\sum_e \kappa(\mathbf{K}_{ij}^e(\mathbf{u}_{ij})) \geq \kappa(\mathbf{K}_{ij}(\mathbf{u}_{ij}))$. Moreover, by definition (see (7)),

$$\nu_{ij}^e \geq \kappa(\mathbf{f}'(\mathbf{u}_{ij}) \cdot (\nabla \varphi_j, \varphi_i)_{K_e}) \quad \text{for } j \neq i.$$

Furthermore, from (6), it is easy to see that $\kappa(\mathbf{B}_{ij}^e(\mathbf{u}_{ij})) \geq \kappa(\mathbf{K}_{ij}^e(\mathbf{u}_{ij}))$, hence $\kappa(\mathbf{B}_{ij}(\mathbf{u}_{ij})) \geq \kappa(\mathbf{K}_{ij}(\mathbf{u}_{ij}))$. Finally, since $\bar{\mathbf{K}}_{ij} = \mathbf{K}_{ij} + \mathbf{B}_{ij}$ and $\mathbf{B}_{ij} = \sum_e \mathbf{B}_{ij}^e = \sum_e -\nu_{ij}^e I_{m \times m}$ for all $j \neq i$, then the maximum eigenvalue of $\bar{\mathbf{K}}_{ij}(\mathbf{u}_{ij})$ is non-positive, which completes the proof. \square

3.1. Differentiability. In the case of steady, or implicit time integration, differentiability plays a role in the convergence behavior of the nonlinear solver. This is specially important if one wants to use Newton's method. In the case of scalar problems it has been shown in [2, 3] that convergence is greatly improved after few modifications to make a scheme twice-differentiable. In this section, we introduce a set of regularizations applied to all non-differentiable functions present in the stabilized scheme introduced above. In order to regularize these functions, we follow a similar strategy as [2, 3]. Absolute values are substituted by

$$|x|_{1, \varepsilon_h} = \sqrt{x^2 + \varepsilon_h}, \quad |x|_{2, \varepsilon_h} = \frac{x^2}{\sqrt{x^2 + \varepsilon_h}}.$$

Note that $|x|_{2, \varepsilon_h} \leq |x| \leq |x|_{1, \varepsilon_h}$. Next, we also use a smooth maximum function, $\max_{\sigma_h}(\cdot)$, as

$$\max_{\sigma_h}(x, y) \doteq \frac{|x - y|_{1, \sigma_h} + x + y}{2} \geq \max(x, y). \quad (12)$$

In addition, we need a smooth function to limit the value of any given quantity to one. To this end, we use

$$Z(x) \doteq \begin{cases} 2x^4 - 5x^3 + 3x^2 + x, & x < 1, \\ 1, & x \geq 1. \end{cases}$$

The set of twice-differentiable functions defined above allows us to redefine the stabilization term introduced in Sect. 3. In particular, we define

$$\tilde{B}_h(\mathbf{w}_h; \mathbf{u}_h, \mathbf{v}_h) \doteq \sum_{K_e \in \mathcal{T}_h} \sum_{i, j \in \mathcal{N}_h(K_e)} \tilde{\nu}_{ij}^e(\mathbf{w}_h) \ell(i, j) \mathbf{v}_i \cdot I_{m \times m} \mathbf{u}_j,$$

where

$$\begin{aligned} \tilde{\nu}_{ij}^e(\mathbf{w}_h) &\doteq \max_{\sigma_h}(\alpha_{\varepsilon_h, i}(\mathbf{w}_h) \lambda_{ij}^{\max}, \alpha_{\varepsilon_h, j}(\mathbf{w}_h) \lambda_{ji}^{\max}), \quad \text{for } j \in \mathcal{N}_h(\Omega_i) \setminus \{i\}, \\ \tilde{\nu}_{ii}^e(\mathbf{w}_h) &\doteq \sum_{j \in \mathcal{N}_h(\Omega_i) \setminus \{i\}} \tilde{\nu}_{ij}^e(\mathbf{w}_h). \end{aligned} \quad (13)$$

Let us note that λ_{ij}^{\max} needs to be regularized as $\lambda_{ij}^{\max} = |\mathbf{v}_{ij} \mathbf{c}_{ij}^e|_{1, \varepsilon_h} + c \|\mathbf{c}_{ij}^e\|$. The shock detector is also redefined to use the regularized version of the shock detector, which reads

$$\alpha_{\varepsilon_h, i}(\mathbf{u}_h) \doteq \max_{\sigma_h} \{\alpha_{\varepsilon_h, i}(u_h^\beta)\}_{\beta \in C}.$$

In the case of the component shock detector we recall the definition in [2, eq. 18]

$$\alpha_{\varepsilon_h, i}(u_h^\beta) \doteq \left[Z \left(\frac{\left| \sum_{j \in \mathcal{N}_h(\Omega_i)} \left[\left\| \nabla u_h^\beta \right\|_{ij} \right]_{1, \varepsilon_h} + \zeta_h}{\sum_{j \in \mathcal{N}_h(\Omega_i)} 2 \left\{ \left\| \nabla u_h^\beta \cdot \hat{\mathbf{r}}_{ij} \right\|_{2, \varepsilon_h} \right\}_{ij} + \zeta_h} \right) \right]^q, \quad (14)$$

where ζ_h is a small value for preventing division by zero. Finally, the twice-differentiable stabilized scheme reads:

Find $\mathbf{u}_h \in \mathbf{V}_h$ such that $u_h^\beta = \bar{u}_h^\beta$ on Γ_{in}^β , $\mathbf{u}_h = \mathbf{u}_{0h}$ at $t = 0$, and

$$\tilde{\mathbf{M}}(\mathbf{u}_h^{n+1}) \delta_t \mathbf{U}^{n+1} + \tilde{\mathbf{K}}(\mathbf{u}_h^{n+1}) \mathbf{U}^{n+1} = \mathbf{G} \quad \text{for } n = 1, \dots, n^{ts}, \quad (15)$$

where

$$\begin{aligned} \tilde{\mathbf{M}}_{ij}(\mathbf{u}_h^{n+1}) &\doteq [1 - \max_{\sigma_h} (\alpha_{\varepsilon_h, i}, \alpha_{\varepsilon_h, j})] (\varphi_j, \varphi_i) I_{m \times m} + \max_{\sigma_h} (\alpha_{\varepsilon_h, i}, \alpha_{\varepsilon_h, j}) (\delta_{ij}, \varphi_i) I_{m \times m}, \\ \tilde{\mathbf{K}}_{ij}(\mathbf{u}_h^{n+1}) &\doteq \mathbf{K}_{ij}(\mathbf{u}_h^{n+1}) + \tilde{\mathbf{B}}_{ij}(\mathbf{u}_h^{n+1}), \end{aligned}$$

and $\tilde{\mathbf{B}}_{ij}(\mathbf{u}_h) \doteq \sum_{K_e \in \mathcal{T}_h} \tilde{\nu}_{ij}^e(\mathbf{u}_h) \ell(i, j) I_{m \times m}$, for $i, j \in \mathcal{N}_h$.

Corollary 3.1. *The differentiable scheme in Eq. (13) is local bounds preserving, as defined in Def. 2.4, at any region where u_h^β has extreme values for every β in C .*

Proof. For an extreme value of u_h^β , since $|x|_{2, \varepsilon_h} \leq |x| \leq |x|_{1, \varepsilon_h}$ the quotient of (14) is larger than one. Hence, by definition of $Z(x)$, $\alpha_{\varepsilon_h, i}$ is equal to 1. At this point, it is easy to check that $\tilde{\nu}_{ij}^e \geq \nu_{ij}^e$ in virtue of the definition of \max_{σ_h} . Therefore, $\kappa(\tilde{\mathbf{B}}_{ij}^e(\mathbf{u}_h)) \geq \kappa(\mathbf{B}_{ij}^e(\mathbf{u}_h))$, completing the proof. \square

Moreover, it is important to mention that the differentiable shock detector is weakly linearly-preserving as ζ_h tends to zero. This result follows directly from [2]. In order to obtain a differentiable operator, we have added a set of regularizations that rely on different parameters, e.g., σ_h , ε_h , ζ_h . Giving a proper scaling of these parameters is essential to recover theoretic convergence rates. In particular, we use the following relations

$$\sigma_h = \sigma |\lambda^{\max}|^2 L^{2(d-3)} h^4, \quad \varepsilon_h = \varepsilon L^{-4} h^2, \quad \zeta_h = L^{-1} \zeta, \quad (16)$$

where d is the spatial dimension of the problem, L is a characteristic length, and σ , ε , and ζ are of the order of the unknown.

4. NONLINEAR SOLVER

In this section, we describe the method used for solving the nonlinear system of equations arising from the scheme introduced above. In particular, we use a hybrid Picard–Newton approach in order to increase the robustness of the nonlinear solver. Moreover, for the differentiable version we also use a continuation method to improve the nonlinear convergence.

We represent the residual of the equation (15) at the k -th iteration by $\mathbf{R}(\mathbf{u}_h^{k, n+1})$, i.e.,

$$\mathbf{R}(\mathbf{u}_h^{k, n+1}) \doteq \tilde{\mathbf{M}}(\mathbf{u}_h^{k, n+1}) \delta_t \mathbf{U}^{k, n+1} + \tilde{\mathbf{K}}(\mathbf{u}_h^{k, n+1}) \mathbf{U}^{k, n+1} - \mathbf{G}. \quad (17)$$

Hence, the Jacobian is defined as

$$\begin{aligned} \mathbf{J}(\mathbf{u}_h^{k, n+1}) &\doteq \frac{\partial \mathbf{R}(\mathbf{u}_h^{k, n+1})}{\partial \mathbf{U}^{k, n+1}} \\ &= \Delta t_{n+1}^{-1} \tilde{\mathbf{M}}(\mathbf{u}_h^{k, n+1}) + \tilde{\mathbf{K}}(\mathbf{u}_h^{k, n+1}) + \Delta t_{n+1}^{-1} \frac{\partial \tilde{\mathbf{M}}(\mathbf{u}_h^{k, n+1})}{\partial \mathbf{U}^{k, n+1}} \delta_t \mathbf{U}^{k, n+1} + \frac{\partial \tilde{\mathbf{K}}(\mathbf{u}_h^{k, n+1})}{\partial \mathbf{U}^{k, n+1}} \mathbf{U}^{k, n+1}. \end{aligned} \quad (18)$$

Therefore, Newton method consists of solving $\mathbf{J}(\mathbf{u}_h^{k, n+1}) \Delta \mathbf{U}^{k+1, n+1} = -\mathbf{R}(\mathbf{u}_h^{k, n+1})$. However, it is well known that Newton method can diverge if the initial guess of the solution $\mathbf{u}_h^{0, n+1}$ is not close enough to the solution. In order to improve the robustness, we introduce the following modifications. We use a line-search method to update the solution at every time step. Thus, the new approximation is

computed as $\mathbf{U}^{k+1,n+1} = \mathbf{U}^{k,n+1} + \lambda \Delta \mathbf{U}^{k+1,n+1}$, where λ is computed (approximately) such that it minimizes $\|\mathbf{R}(\mathbf{u}_h^{k+1,n+1})\|$. To approximate λ we use a standard golden section search algorithm [9]. However, any other minimization or backtracking strategy could potentially be used.

As introduced at the beginning of the section, we also use a hybrid approach combining Newton method with Picard linearization. Picard nonlinear iterator can be obtained removing the last two terms of (18), i.e.,

$$\left(\Delta t_{n+1}^{-1} \tilde{\mathbf{M}}(\mathbf{u}_h^{k,n+1}) + \tilde{\mathbf{K}}(\mathbf{u}_h^{k,n+1}) \right) \Delta \mathbf{U}^{k+1,n+1} = -\mathbf{R}(\mathbf{u}_h^{k,n+1}). \quad (19)$$

Clearly, it is equivalent to

$$\left(\Delta t_{n+1}^{-1} \tilde{\mathbf{M}}(\mathbf{u}_h^{k,n+1}) + \tilde{\mathbf{K}}(\mathbf{u}_h^{k,n+1}) \right) \mathbf{U}^{k+1,n+1} = \tilde{\mathbf{M}}(\mathbf{u}_h^{k,n+1}) \mathbf{U}^n + \mathbf{G}.$$

Moreover, we modify the definition of left hand side terms in (19) to enhance the robustness of the method. In particular, we use $\alpha_i = 1$ for computing these terms while we use the value obtained from (9) for the residual. Using this strategy the solution remains unaltered, but the obtained approximations $\mathbf{u}_h^{k,n+1}$ for intermediate values of k are more diffusive. Even though this modification slows the nonlinear convergence, it is essential at the initial iterations. Otherwise, the robustness of the method might be jeopardized.

The resulting iterative nonlinear solver consists in the following. We iterate using Picard method in (19), with the modification described above, until the L^2 norm of the residual is smaller than a given tolerance. In the present work, we use tolerances close to 10^{-2} . Afterwards, Newton method with the exact Jacobian in (18) is used until the desired nonlinear convergence criteria are satisfied.

For the differentiable stabilization, we also equip the above scheme with a continuation method on the regularization parameters. In order to accelerate the convergence of the method, we use high values for the parameters during the first iterations. This results in a more diffusive solution, but nonlinear convergence is accelerated. As the nonlinear approximation is closer to the solution, we diminish the value of the parameters to avoid introducing excessive artificial diffusion to the system. This process is preformed gradually as a function of the residual in (17). In particular, we use the following relation

$$\varepsilon^k = \tilde{\varepsilon} \frac{\|\mathbf{R}(\mathbf{u}_h^{k,n+1})\|}{\|\mathbf{R}(\mathbf{u}_h^{0,n+1})\|},$$

where ε^k is the effective parameter used in relations 16, and $\tilde{\varepsilon}$ is parameter defined by the user. We summarize the nonlinear solver introduced above in Alg. 1.

5. NUMERICAL EXPERIMENTS

In this section, we perform several numerical experiments to assess the numerical scheme introduced in the previous sections. First, we perform a convergence analysis to assess its implementation. Then, we use a steady benchmark test to analyze the effectiveness of the regularization parameters. We also analyze their effectiveness in the case of a transient problem. Finally, we solve a slightly more challenging steady benchmark test.

In all experiments below we assume that the ideal gas state equation applies, and we use an adiabatic index of $\gamma = 1.4$. From previous experience [2, 3, 7, 8], the effects of parameters σ and ε to the nonlinear convergence and numerical error are analogous. Hence, we consider $\varepsilon = 10^{-2}\sigma$. In addition, for all the tests below, the density is discontinuous at all shocks. Therefore, we use $C = \{1\}$ in (9), i.e. the shock detector is based on the density behavior.

5.1. Convergence test. We use two different problems to assess the convergence rate of the scheme. One has a smooth solution, whereas in the other there is a shock. The smooth problem is simply the translation of a sinusoidal perturbation in the density, with constant pressure and velocity. In

```

Input:  $\mathbf{U}^{0,n+1}$ ,  $\text{tol}_1$ ,  $\text{tol}_2$ ,  $\varepsilon$ , Continuation
Output:  $\mathbf{U}^{k,n+1}$ ,  $k$ 
 $k = 1$ ,  $\varepsilon^1 = \varepsilon$ 
while  $\|\mathbf{R}(\mathbf{U}^{k,n+1})\|/\|\mathbf{R}(\mathbf{U}^{0,n+1})\| \geq \text{tol}_1$  do
  Compute  $\alpha_i(\mathbf{U}^{k,n+1})$  using (9)
  Compute  $\Delta\mathbf{U}^{k+1,n+1}$  using (19)
  Minimize  $\|\mathbf{R}(\mathbf{U}^{k+1,n+1})\|$ , where  $\mathbf{U}^{k+1,n+1} = \lambda\Delta\mathbf{U}^{k+1,n+1} + \mathbf{U}^{k,n+1}$ , with respect to  $\lambda$ 
  Set  $\mathbf{U}^{k+1,n+1} = \lambda\Delta\mathbf{U}^{k+1,n+1} + \mathbf{U}^{k,n+1}$ 
  if Continuation then
    Set  $\varepsilon^k = \tilde{\varepsilon} \frac{\|\mathbf{R}(\mathbf{U}^{k+1,n+1})\|}{\|\mathbf{R}(\mathbf{U}^{0,n+1})\|}$ 
  else
    Set  $\varepsilon^k = \varepsilon$ 
  end
  Set  $\sigma^k = 10^2 \varepsilon^k$ 
  Update  $k = k + 1$ 
end
while  $\|\mathbf{R}(\mathbf{U}^{k,n+1})\|/\|\mathbf{R}(\mathbf{U}^{0,n+1})\| \geq \text{tol}_2$  do
  Compute  $\alpha_i(\mathbf{U}^{k,n+1})$  using (9)
  Solve  $\mathbf{J}(\mathbf{U}^{k,n+1})\Delta\mathbf{U}^{k+1,n+1} = -\mathbf{R}(\mathbf{U}^{k,n+1})$  with  $\mathbf{J}$  in (18)
  Minimize  $\|\mathbf{R}(\mathbf{U}^{k+1,n+1})\|$ , where  $\mathbf{U}^{k+1,n+1} = \lambda\Delta\mathbf{U}^{k,n+1} + \mathbf{U}^{k,n+1}$ , with respect to  $\lambda$ 
  Set  $\mathbf{U}^{k+1,n+1} = \lambda\Delta\mathbf{U}^{k,n+1} + \mathbf{U}^{k,n+1}$ 
  if Continuation then
    Set  $\varepsilon^k = \tilde{\varepsilon} \frac{\|\mathbf{R}(\mathbf{U}^{k+1,n+1})\|}{\|\mathbf{R}(\mathbf{U}^{0,n+1})\|}$ 
  else
    Set  $\varepsilon^k = \varepsilon$ 
  end
  Set  $\sigma^k = 10^2 \varepsilon^k$ 
  Update  $k = k + 1$ 
end

```

Algorithm 1: Hybrid Picard–Newton scheme with the continuation method.

particular, the solution for $r = \sqrt{(0.5 + t - x)^2 + (0.5 - y)^2} < 0.5$ is

$$\mathbf{u} = \begin{bmatrix} \rho \\ v_1 \\ v_2 \\ p \end{bmatrix} = \begin{bmatrix} 1 + 0.9999 \cos(2\pi r) \\ 1 \\ 0 \\ 1 \end{bmatrix},$$

and $\mathbf{u} = [0.0001, 1, 0, 1]^t$ otherwise.

The non-smooth problem is the well known compression corner test [1, 27], also known as oblique shock test [36, 39]. This benchmark consists in a supersonic flow impinging to a wall at an angle. We use a $[0, 1]^2$ domain with a $M = 2$ flow at 10° with respect to the wall. This leads to two flow regions separated by an oblique shock at 29.3° , see the scheme in Fig. 2.

For both tests, we compare the convergence rates for the differentiable and the non-differentiable schemes. q is set to 10 and the regularization parameters are $\gamma = 10^{-10}$, $\varepsilon = 10^{-4}$, and $\sigma = 10^{-2}$ in the differentiable version. The convergence criterion for both tests is $\frac{\|\Delta\mathbf{u}_h^{k+1}\|}{\|\mathbf{u}_h^k\|} < 10^{-6}$. The scheme is able to converge in less than 10 iterations for the smooth problem, regardless of the setting or the mesh used. However, for the compression corner some tests did not converge. In this case, the iteration limit is set to 150. Nevertheless, $\frac{\|\Delta\mathbf{u}_h^{k+1}\|}{\|\mathbf{u}_h^k\|} \ll \|\rho - \rho_h\|_{L^1(\Omega)}$ is always checked and satisfied for all tests.

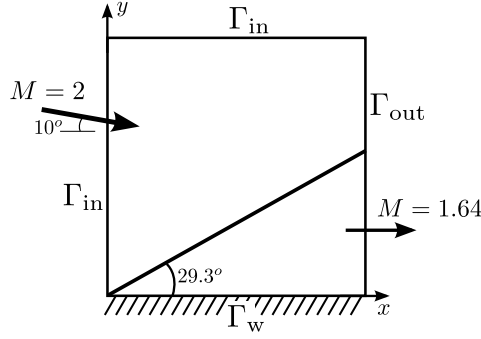


FIGURE 2. Compression corner scheme.

In Fig. 3, the L^1 error is depicted for different mesh sizes, and in Tab. 1 we collect the measured convergence rates. It can be observed that for a smooth problem both settings recover second order convergence, whereas for non-smooth problems the expected first order convergence rates are obtained. For this particular choice of regularization parameters, we observe that the errors are slightly higher. However, the convergence rates are not affected by the regularization described in Sect. 3.1.

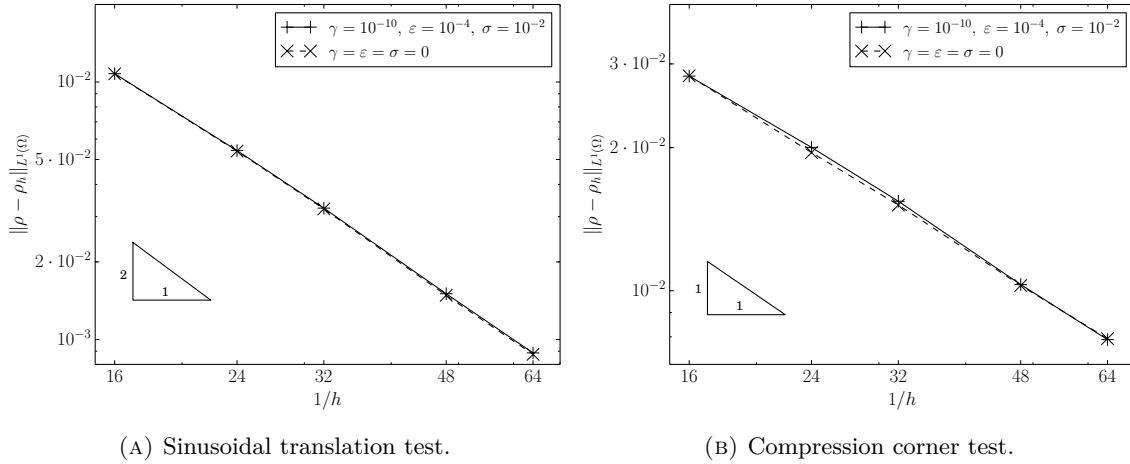


FIGURE 3. Density convergence for successive mesh refinements.

TABLE 1. Experimental convergence rates for both problems.

Test	L_1 error
Sinusoidal translation (differentiable)	1.8099
Sinusoidal translation (non-differentiable)	1.8190
Compression corner (differentiable)	0.9278
Compression corner (non-differentiable)	0.9207

5.2. Reflected Shock. In this test, we compare the nonlinear convergence behavior of the method for different regularization parameters. This benchmark consists in two flow streams colliding at different angles. The domain has dimensions $[0.0, 1.0] \times [0.0, 4.1]$ and a solid wall at its lower boundary. This configuration leads to a steady shock separating both flow regimes, which in turn, is reflected at the wall producing a third different flow state behind it. A sketch of this benchmark test is given in Fig. 4. The flow states at each region have been collected in Tab. 2.

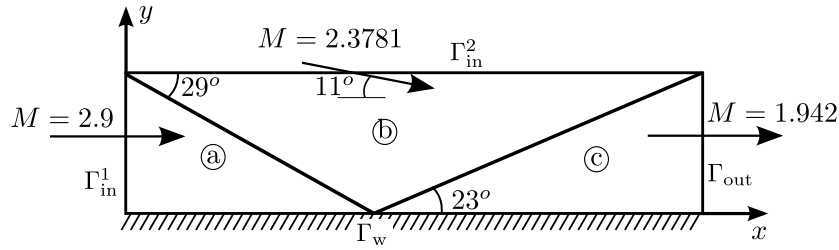


FIGURE 4. Reflected shock scheme.

TABLE 2. Reflected shock solution values at every region.

Region	Density [Kg m ⁻³]	Velocity [m s ⁻¹]	Total energy [J]
Ⓐ	1.0	(2.9, 0.0)	5.99075
Ⓑ	1.7	(2.62, -0.506)	5.8046
Ⓒ	2.687	(2.401, 0.0)	5.6122

We use a 60×20 structured \mathcal{Q}_1 mesh. The problem is solved directly to steady state using the hybrid method and the continuation scheme described in Sect. 4. The tolerance used for switching from Picard to Newton linearization is 10^{-2} . We compare the convergence behavior for $q = \{1, 2, 5, 10\}$. For the differentiable stabilization we use the following values for $\tilde{\varepsilon} = \{10^{-4}, 10^{-2}, 1\}$. We consider $\varepsilon^k = \sigma^k 10^{-2}$. The value of γ is 10^{-10} .

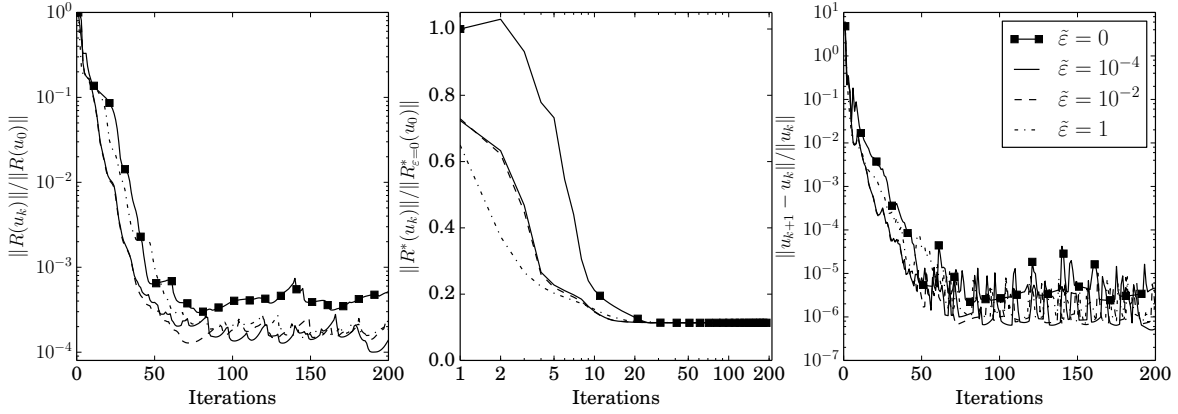
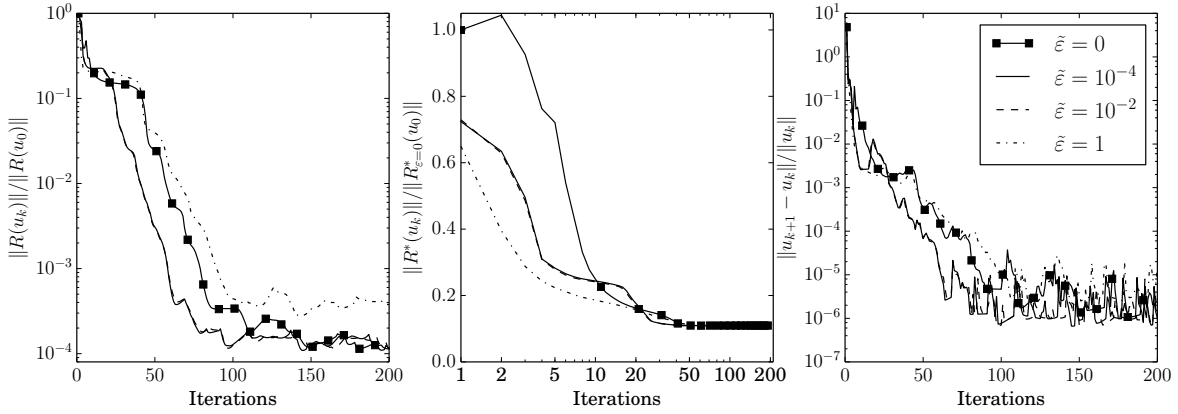
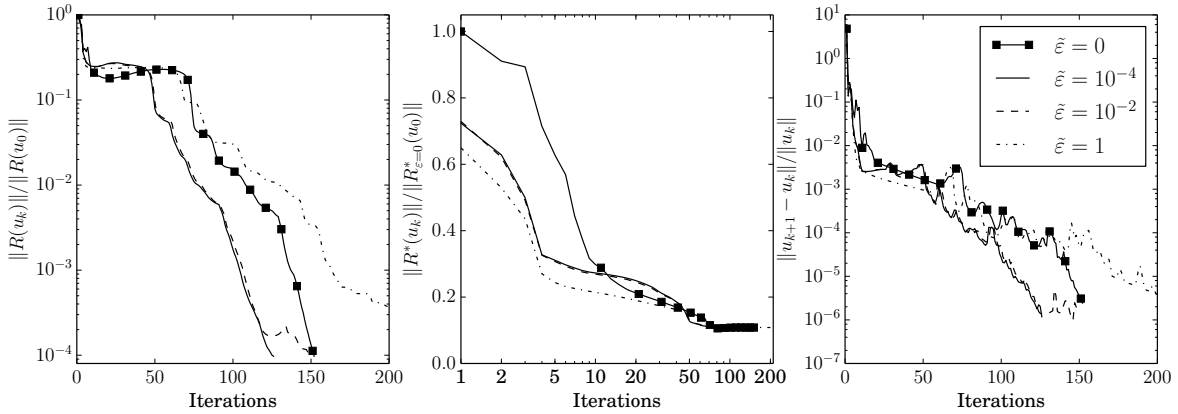
In Figs. 5-8 for every nonlinear iteration we depict (from left to right) the relative residual, the relative Galerkin residual, and the relative solution variation between iterations. The Galerkin residual is simply the residual in (17) minus the stabilization terms, i.e.,

$$\mathbf{R}^*(\mathbf{u}_h^k) \doteq \mathbf{K}(\mathbf{u}_h^k) \mathbf{U}^k - \mathbf{G}.$$

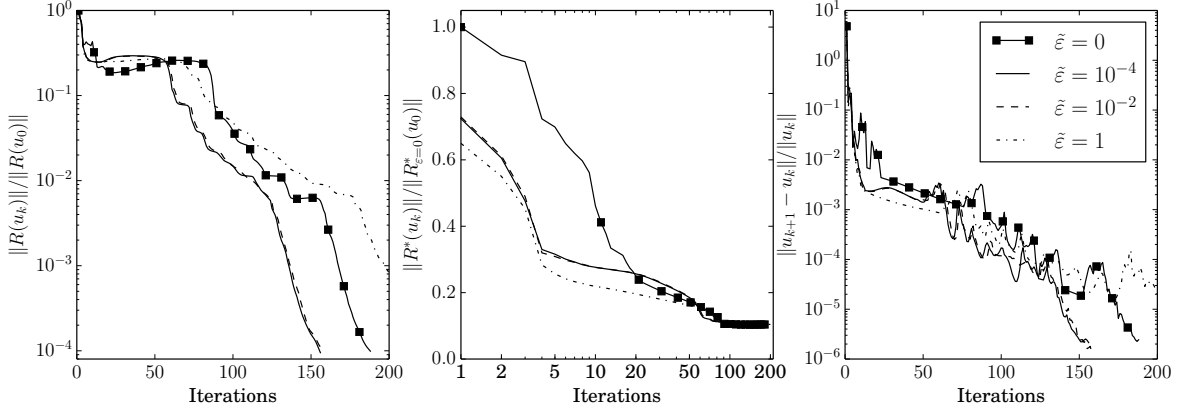
We depict this value relative to the Galerkin residual of the non-differentiable scheme. This value gives a sense of how close is the computed approximation to the solution of the original problem. However, since it omits the stabilization terms present in the system solved, it will stagnate at some point.

In general, we can observe in Figs. 5-8 that as q is increased nonlinear convergence rates are reduced. For instance, one can observe that the higher is q the more iterations the scheme needs to reach $\|\mathbf{R}(\mathbf{u}_h^{k+1})\|/\|\mathbf{R}(\mathbf{u}_h^0)\| < 10^{-3}$. Unfortunately, using a low value of q might also make the scheme to stagnate before reaching convergence. This is observed in Figs. 5 and 6. In addition, we observe a 15% to 35% reduction in the number of iterations when the differentiable scheme is used. Another interesting observation is about the behavior of the Galerkin residual. This residual is not expected to converge since we are not solving the original problem but the stabilized one. However, it provides an indication of how close to the original solution is the one obtained by the proposed scheme. During the first iterations, the differentiable scheme is able to provide solutions closer to the solution of the original problem. This implies that, up to some extent, the differentiable scheme is able to provide more accurate solutions from the beginning of the iterative process. It is also interesting to observe the improvement in the residual convergence once the complete Jacobian is used, i.e. after $\|\mathbf{R}(\mathbf{u}_h^{k+1})\|/\|\mathbf{R}(\mathbf{u}_h^0)\| < 10^{-2}$. This is specially evident in Figs. 7-8.

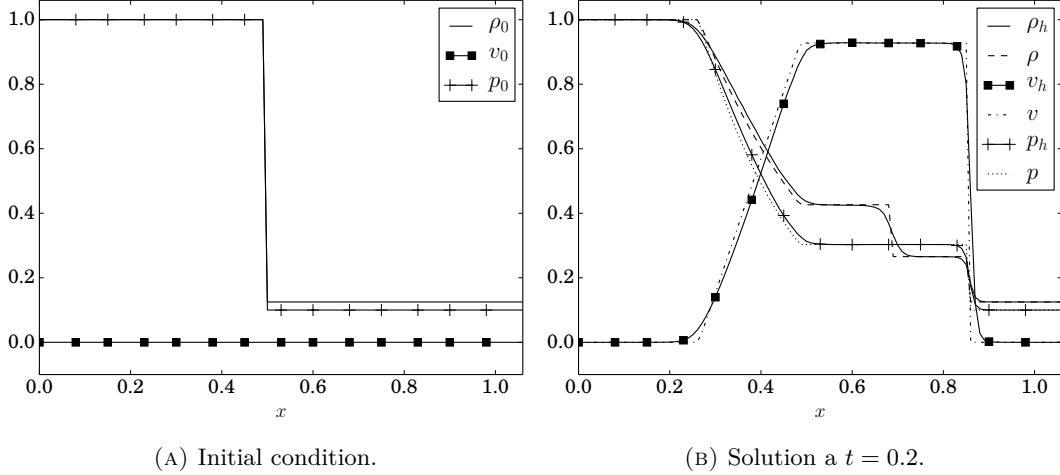
5.3. Sod's Shock Tube. In this section, we evaluate the effect of the differentiability in the case of a transient problem. To this end, we solve the well known Sod's shock tube test. This is a one dimensional problem that assesses the evolution of a fluid initially at rest with a discontinuity in density and pressure. The discontinuity is initially placed at $x = 0.5$. Even though it is a 1D test, we consider a narrow 2D strip of dimensions $[0, 1] \times [0, 0.01]$ and we let the problem evolve until $t = 0.2$. We use a \mathcal{Q}_1 FE mesh of size $\Delta x = 0.01$ and a time step length of $\Delta t = 0.001$. Initial conditions at the left of the discontinuity are $\mathbf{u}_0 = (1, 0, 0, 2.5)$ and at the right $\mathbf{u}_0 = (0.125, 0, 0, 0.25)$. See the initial condition depicted in Fig. 9a.

FIGURE 5. Reflected shock convergence history for $q = 1$.FIGURE 6. Reflected shock convergence history for $q = 2$.FIGURE 7. Reflected shock convergence history for $q = 5$.

In this case, the hybrid nonlinear solver described in Sect. 4 is used directly without the continuation scheme. The tolerance used for switching from the Picard to Newton linearization is $5 \cdot 10^{-3}$. We set

FIGURE 8. Reflected shock convergence history for $q = 10$.

the nonlinear convergence criteria in terms of the relative residual, namely $\frac{\|\mathbf{R}(\mathbf{u}_h^{k,n+1})\|}{\|\mathbf{R}(\mathbf{u}_h^{0,n+1})\|} < 10^{-6}$. We use $\gamma = 10^{-10}$, $\varepsilon = \{10^{-2}, 10^{-3}, 10^{-4}, 10^{-5}\}$, and $\varepsilon = \sigma 10^{-2}$ for the differentiable stabilization. We also use different values of q for this comparison, namely $q = \{1, 2, 4, 6, 8, 10, 12\}$.



(A) Initial condition.

(B) Solution at $t = 0.2$.FIGURE 9. Sod shock initial condition and solution for the differentiable scheme using parameters $q = 10$, $\sigma = 10^{-3}$, $\varepsilon = 10^{-5}$, and $\gamma = 10^{-10}$.

Fig. 9b shows a comparison at $t = 0.2$ of the exact solution from ExactPack [37] against the obtained solution for $q = 10$, $\sigma = 10^{-3}$, $\varepsilon = 10^{-5}$, and $\gamma = 10^{-10}$. In this case, we observe a good agreement of the obtained solution despite the rather coarse mesh being used.

In Fig. 10, for different regularization values, we depict the total number of nonlinear iterations required to reach $t = 0.2$, and the density error L^1 norm, as a function of the value of q . For each chart, we compare the results for the differentiable and non-differentiable stabilization. Analyzing these figures, several general observations can be made. One recovers the behavior of the non-differentiable scheme as the parameters used in the differentiable scheme become smaller (see 10d). Using large values for the regularization parameters improves the computational cost required at the expense of higher numerical errors (see 10a). It can also be seen that for transient problems the benefits of differentiability are not as evident as for problems solved directly to steady state. Notice that the differentiable scheme always require less iterations to converge. However the difference is smaller than

for steady state problems as one would expect since the time advancement provides a decrease in the effective regularization by the existence of the time derivative and the evolution of the transient problem at each time step.

Another interesting observation can be made when moderate values for the parameters are used. Namely, the differentiable scheme is able to yield results with a similar accuracy while requiring a lower computational cost. For example, let us focus on Fig. 10b and compare the performance of the differentiable scheme for $q = 2$ and the non-differentiable with $q = 1$. The first observation is that both settings have similar accuracy. However, the differentiable scheme converges faster. If we focus on Fig. 10c similar observations can be made. For instance, compare the performance of the differentiable scheme with $q = 4$ and the non-differentiable with $q = 2$. The differentiable scheme is able to yield a more accurate solution in less iterations. Therefore, one can come to the conclusion that in order to achieve a given accuracy it is preferable to use the differentiable scheme with a slightly larger value of q rather than the non-differentiable scheme and a lower value for q .

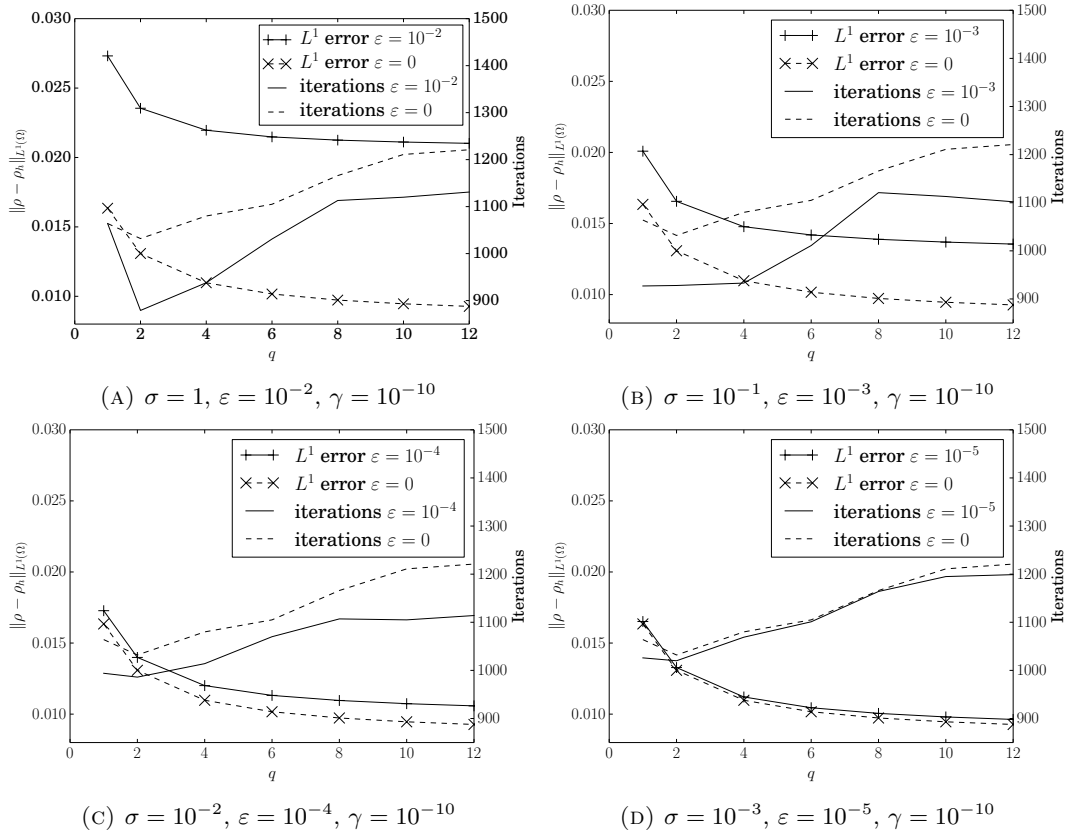


FIGURE 10. Comparison of L^1 error and computational cost (total number of iterations) for different regularization parameters choices at the Sod's shock test.

5.4. Scramjet. Finally, we solve a problem with a supersonic flow that develops a complex shock pattern. This test consists of a $M = 3$ channel that narrows along the streamline and has two internal obstacles. In particular, Fig. 11 is an illustration of the domain and Tab. 3 lists the coordinates of the points defining the domain. The problem is solved directly to steady state, and two different meshes have been used. The coarsest mesh used has 18476 \mathcal{Q}_1 elements and the finest mesh has 63695 \mathcal{Q}_1 elements.

In order to solve this problem, the hybrid nonlinear solver described in Sect. 4 is used with the help of the continuation scheme. The tolerance for switching from the Picard to Newton linearization is set

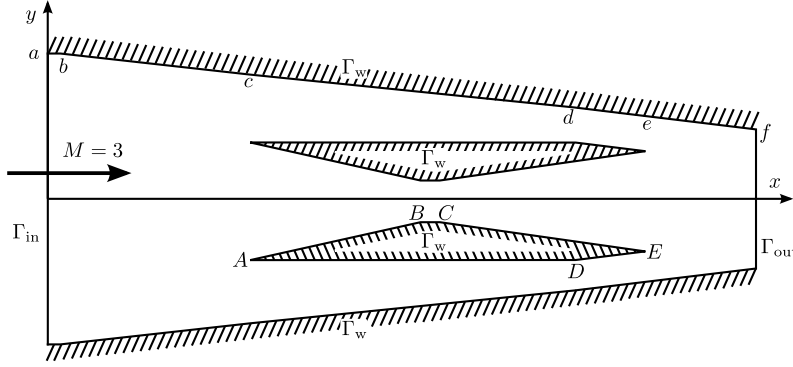


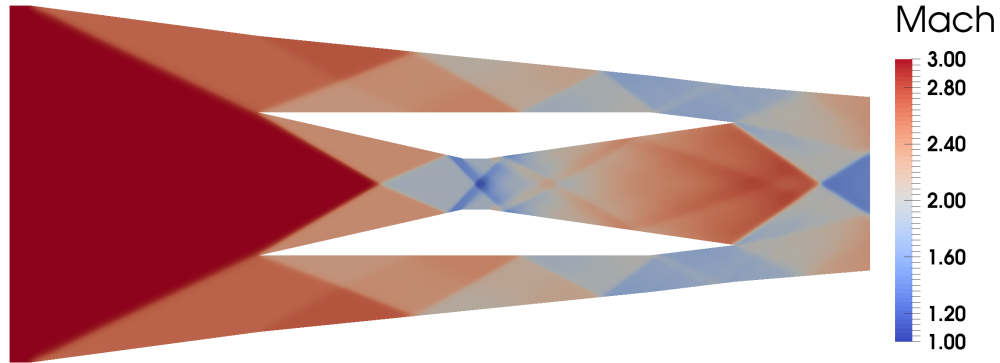
FIGURE 11. Scramjet test scheme.

TABLE 3. Domain coordinates for the scramjet test.

Wall	a	b	c	d	e	f
x_i	0.0	0.4	4.9	12.6	14.25	16.9
y_i	3.5	3.5	2.9	2.12	1.92	1.7
Interior obstacle	A	B	C	D	E	
x_i	4.9	8.9	9.4	12.6	14.25	
y_i	-1.4	-0.5	-0.5	-1.4	-1.2	

to $5 \cdot 10^{-2}$. The nonlinear convergence criterion for this benchmark is $\frac{\|\Delta(\mathbf{u}_h^{k+1})\|}{\|\mathbf{u}_h^k\|} < 10^{-6}$. We also set a maximum number of iterations of 500. In this test, we use $q = \{2, 5\}$, $\gamma = 10^{-10}$, $\tilde{\varepsilon} = \{1, 10^{-2}, 10^{-4}\}$, and $\varepsilon^k = \sigma^k 10^{-2}$. Even though $\sigma = 10^2$ might seem a high value, we recall that it is used in the context of a continuation method. Therefore, the effective value of σ^k is lower than 1 for the converged solution. Moreover, the actual value used in (12) is computed using the relations in (16).

Figs. 12-13 show, respectively, the Mach and density contours for the fine mesh, $q = 5$, $\tilde{\varepsilon} = 1$, $\tilde{\varepsilon} = 10^2$, and $\gamma = 10^{-10}$. The nonlinear convergence history for this configuration is depicted in Figs. 17c-17d. The obtained values for the Mach number and the density are comparable to those in [27, 34]. The shocks are well resolved. Even when using $q = 2$ the shocks are properly resolved and only slightly more smeared than for $q = 5$, see Fig. 14. If instead, the coarse mesh is used (see Fig. 15), the solution is more dissipative. However, the scheme is able to capture most of the features present in the solution.

FIGURE 12. Scramjet Mach contours when a mesh of 63695 \mathcal{Q}_1 elements is used, with parameters $q = 5$, $\gamma = 10^{-10}$, and $\tilde{\varepsilon} = 1$.

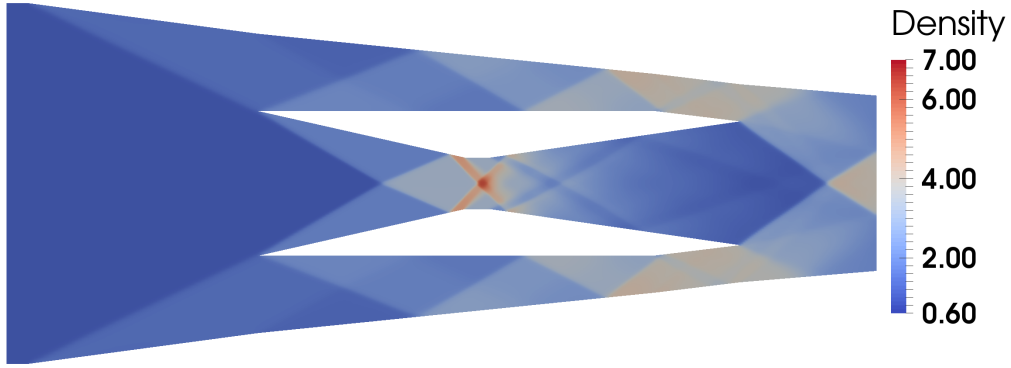


FIGURE 13. Scramjet density contours when a mesh of 63695 Q_1 elements is used, with parameters $q = 5$, $\gamma = 10^{-10}$, and $\tilde{\varepsilon} = 1$.

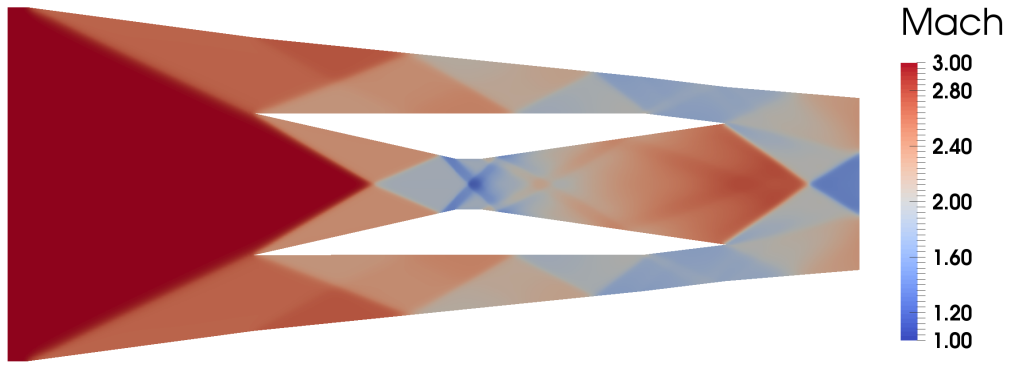


FIGURE 14. Scramjet Mach contours when a mesh of 63695 Q_1 elements is used, with parameters $q = 2$, $\gamma = 10^{-10}$, and $\tilde{\varepsilon} = 1$.

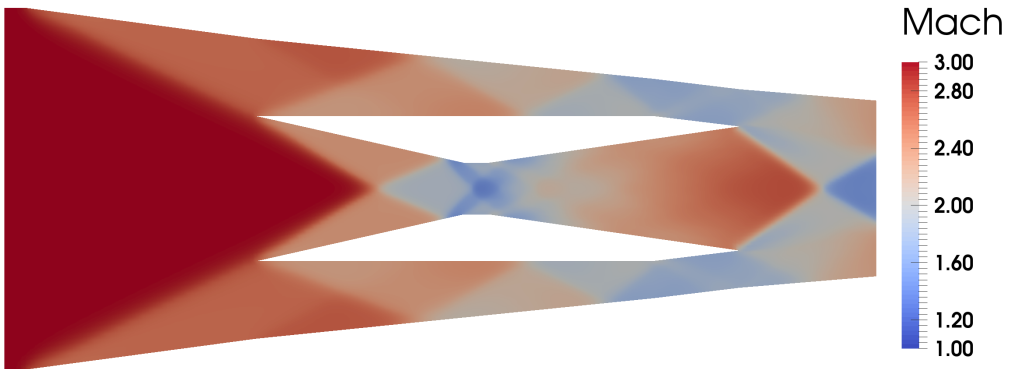


FIGURE 15. Scramjet Mach contours when a mesh of 18476 Q_1 elements is used, with parameters $q = 2$, $\gamma = 10^{-10}$, and $\tilde{\varepsilon} = 1$.

Figs. 16-17 show the nonlinear convergence history in terms of the relative residual reduction and the relative solution increment between iterations. We can observe that the convergence is not ensured

for an arbitrary choice of the regularization parameters. In fact, only the tests that use $\tilde{\varepsilon} = 1$ do not diverge for $q = 5$, regardless of the mesh used. Therefore, we can see that increasing the values of the regularization parameters not only improves the convergence, but also the robustness of the method.

However, it is important to mention that even if we can improve the convergence behavior of these types of methods, this is not enough for directly solving to steady state problems with complex shock patterns. For instance, even if the solution of Fig. 15 seems to be correct, the scheme was unable to converge to the desired tolerance (see Figs. 16c and 16d). However the ability to introduce differentiability into the definition of the shock detector, for robustness and increased nonlinear convergence rates, could be coupled with popular pseudo-time stepping approaches [21, 38] to pursue improved methods for complex shock type systems.

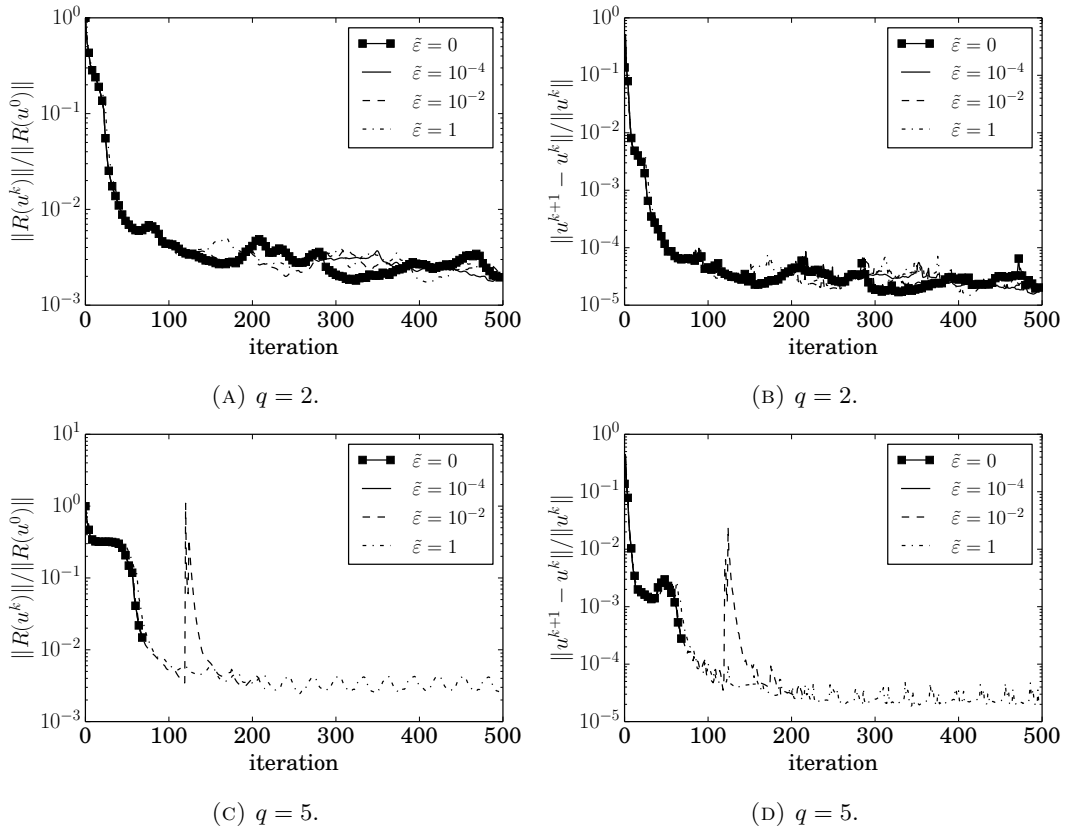


FIGURE 16. Comparison of the convergence behavior for the Scramjet test and different regularization parameters choices. A coarse mesh of 18476 \mathcal{Q}_1 elements is used.

6. CONCLUSIONS

In this work, a differentiable *local bounds preserving* stabilization for Euler equations was presented. This stabilization is based on the combination of a differentiable shock detector, a partially lumped mass matrix, and Rusanov artificial diffusion. The scheme has been successfully tested in steady and transient benchmark problems. Numerical results show that the proposed method exhibits good stability properties. Application of the scheme to steady and transient problems with shocks resulted in well resolved profiles. In addition the differentiable shock detector, a continuation method for the regularization parameters in the differentiable stabilization was presented. This was done to improve nonlinear convergence. Nonlinear convergence of the scheme was then analyzed for the differentiable version was compared to that of the non-regularized counterpart. The differentiable stabilization

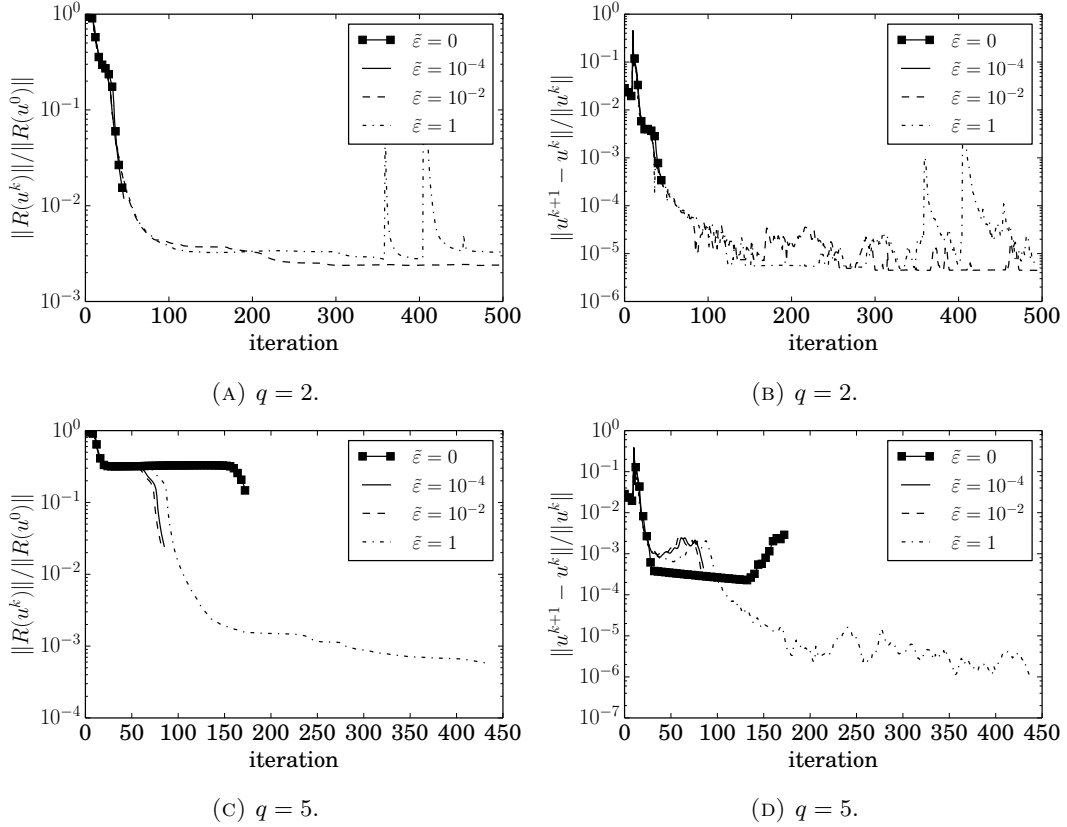


FIGURE 17. Comparison of the convergence behavior for the Scramjet test and different regularization parameters choices. A fine mesh of 63695 \mathcal{Q}_1 elements is used.

showed better convergence, especially when the hybrid Picard–Newton method was used. For small steady problems, the scheme is able to converge directly to the steady state solution without making use of pseudo-transient time stepping. However, for problems with complex shock patterns the scheme only converges to moderate tolerances. Numerical results also show that differentiability not only improves nonlinear convergence, but also improves the robustness of the method. In the case of transient problems, some improvement in the computational cost is observed. However, since the non-differentiable method already exhibits good nonlinear convergence, there is not much room for improvement. Nevertheless, it is possible to show that the differentiable stabilization can achieve a similar accuracy while lowering the computational cost.

ACKNOWLEDGMENTS

The work of S. Mabuza and J.N. Shadid was partially supported by the U.S. Department of Energy, Office of Science, Office of Applied Scientific Computing Research. Sandia National Laboratories is a multi-mission laboratory managed and operated by National Technology and Engineering Solutions of Sandia, LLC., a wholly owned subsidiary of Honeywell International, Inc., for the U.S. Department of Energy’s National Nuclear Security Administration under contract DE-NA0003525. This paper describes objective technical results and analysis. Any subjective views or opinions that might be expressed in the paper do not necessarily represent the views of the U.S. Department of Energy or the United States Government. J. Bonilla gratefully acknowledges the support received from “la Caixa” Foundation through its PhD scholarship program (LCF/BQ/DE15/10360010). S. Badia gratefully

acknowledges the support received from the Catalan Government through the ICREA Acadèmia Research Program. S. Badia and J. Bonilla also acknowledge the financial support to CIMNE via the CERCA Programme / Generalitat de Catalunya.

REFERENCES

- [1] J. D. ANDERSON JR., *Modern Compressible Flow*, McGraw-Hill, 2nd ed., 1990.
- [2] S. BADIA AND J. BONILLA, *Monotonicity-preserving finite element schemes based on differentiable nonlinear stabilization*, *Computer Methods in Applied Mechanics and Engineering*, 313 (2017), pp. 133–158.
- [3] S. BADIA, J. BONILLA, AND A. HIERRO, *Differentiable monotonicity-preserving schemes for discontinuous Galerkin methods on arbitrary meshes*, *Computer Methods in Applied Mechanics and Engineering*, 320 (2017), pp. 582–605.
- [4] S. BADIA AND A. F. MARTÍN, *A tutorial-driven introduction to the parallel finite element library FEMPAR v1.0.0*, *Computer Physics Communications*, 248 (2020), p. 107059.
- [5] S. BADIA, A. F. MARTÍN, AND J. PRINCIPE, *FEMPAR: An Object-Oriented Parallel Finite Element Framework*, *Archives of Computational Methods in Engineering*, 25 (2018), pp. 195–271.
- [6] G. R. BARRENECHEA AND P. KNOBLOCH, *Analysis of a group finite element formulation*, *Applied Numerical Mathematics*, 118 (2017), pp. 238–248.
- [7] J. BONILLA AND S. BADIA, *Maximum-principle preserving space–time isogeometric analysis*, *Computer Methods in Applied Mechanics and Engineering*, 354 (2019), pp. 422–440.
- [8] J. BONILLA, S. MABUZA, J. N. SHADID, AND S. BADIA, *On Differentiable Linearity and Local Bounds Preserving Stabilization Methods for First Order Conservation Law Systems*, in *Center for Computing Research Summer Proceedings 2018*, A. Cangi and M. L. Parks, eds., Sandia National Laboratories, 2018, pp. 107–119.
- [9] R. P. BRENT, *Algorithms for minimization without derivatives*, Prentice-Hall, 1972.
- [10] B. COCKBURN AND C.-W. SHU, *Runge-Kutta Discontinuous Galerkin Methods for Convection-Dominated Problems*, *Journal of Scientific Computing*, 16 (2001), pp. 173–261.
- [11] R. CODINA, *A discontinuity-capturing crosswind-dissipation for the finite element solution of the convection-diffusion equation*, *Computer Methods in Applied Mechanics and Engineering*, 110 (1993), pp. 325–342.
- [12] M. FEISTAUER, J. FELCMAN, AND I. STRAŠKRABA, *Mathematical and computational methods for compressible flow*, Oxford University Press, 2003.
- [13] C. FLETCHER, *The group finite element formulation*, *Computer Methods in Applied Mechanics and Engineering*, 37 (1983), pp. 225–244.
- [14] H. FRID, *Maps of Convex Sets and Invariant Regions for Finite-Difference Systems of Conservation Laws*, *Archive for Rational Mechanics and Analysis*, 160 (2001), pp. 245–269.
- [15] S. GOTTLIEB, C.-W. SHU, AND E. TADMOR, *Strong Stability-Preserving High-Order Time Discretization Methods*, *SIAM Review*, 43 (2001), pp. 89–112.
- [16] J.-L. GUERMOND AND B. POPOV, *Invariant domains and first-order continuous finite element approximation for hyperbolic systems*, (2015), pp. 1–22.
- [17] J.-L. GUERMOND, B. POPOV, AND I. TOMAS, *Invariant domain preserving discretization-independent schemes and convex limiting for hyperbolic systems*, (2018).
- [18] M. GURRIS, *Implicit finite element schemes for compressible gas and particle-laden gas flows*, PhD thesis, Technische Universität Dortmund, 2009.
- [19] D. HOFF, *A finite difference scheme for a system of two conservation laws with artificial viscosity*, *Mathematics of Computation*, 33 (1979), pp. 1171–1171.
- [20] —, *Invariant regions for systems of conservation laws*, *Transactions of the American Mathematical Society*, 289 (1985), pp. 591–591.
- [21] C. T. KELLEY AND D. E. KEYES, *Convergence Analysis of Pseudo-Transient Continuation*, *SIAM Journal on Numerical Analysis*, 35 (1998), pp. 508–523.

- [22] A. KRITZ AND D. KEYES, *Fusion Simulation Project Workshop Report*, Journal of Fusion Energy, 28 (2009), pp. 1–59.
- [23] D. KUZMIN, *Linearity-preserving flux correction and convergence acceleration for constrained Galerkin schemes*, Journal of Computational and Applied Mathematics, 236 (2012), pp. 2317–2337.
- [24] ———, *Monolithic convex limiting for continuous finite element discretizations of hyperbolic conservation laws*, Computer Methods in Applied Mechanics and Engineering, 361 (2020), p. 112804.
- [25] D. KUZMIN, R. LÖHNER, AND S. TUREK, *Flux-corrected transport*, Springer, 2005.
- [26] D. KUZMIN AND M. MÖLLER, *Algebraic Flux Correction I. Scalar Conservation Laws*, in Flux-Corrected Transport, D. D. Kuzmin, P. R. Löhner, and P. D. S. Turek, eds., Scientific Computation, Springer Berlin Heidelberg, jan 2005, pp. 155–206.
- [27] D. KUZMIN, M. MÖLLER, AND M. GURRIS, *Algebraic Flux Correction II. Compressible flows*, in Flux-corrected Transport: Principles, Algorithms, and Applications, 2012, pp. 193–238.
- [28] D. KUZMIN, M. MÖLLER, AND S. TUREK, *Multidimensional FEM-FCT schemes for arbitrary time stepping*, International Journal for Numerical Methods in Fluids, 42 (2003), pp. 265–295.
- [29] D. KUZMIN AND S. TUREK, *Flux Correction Tools for Finite Elements*, Journal of Computational Physics, 175 (2002), pp. 525–558.
- [30] R. J. LEVEQUE, *Finite Volume Methods for Hyperbolic Problems*, Cambridge University Press, Cambridge, 2002.
- [31] C. LOHMANN AND D. KUZMIN, *Synchronized flux limiting for gas dynamics variables*, Journal of Computational Physics, 326 (2016), pp. 973–990.
- [32] R. LOHNER, *Applied Computational Fluid Dynamics Techniques: An Introduction Based on Finite Element Methods*, vol. 508, 2004.
- [33] S. MABUZA, J. N. SHADID, E. C. CYR, R. P. PAWLOWSKI, AND D. KUZMIN, *A linearity preserving nodal variation limiting algorithm for continuous Galerkin discretization of ideal MHD equations*, Journal of Computational Physics, 410 (2020), p. 109390.
- [34] S. MABUZA, J. N. SHADID, AND D. KUZMIN, *Local bounds preserving stabilization for continuous Galerkin discretization of hyperbolic systems*, Journal of Computational Physics, 361 (2018), pp. 82–110.
- [35] P. ROE, *Approximate Riemann solvers, parameter vectors, and difference schemes*, Journal of Computational Physics, 43 (1981), pp. 357–372.
- [36] F. SHAKIB, T. J. R. HUGHES, AND Z. JOHAN, *A new finite element formulation for computational fluid dynamics: X. The compressible Euler and Navier-Stokes equations*, Computer Methods in Applied Mechanics and Engineering, 89 (1991), pp. 141–219.
- [37] R. J. SINGLETON, D. M. ISRAEL, S. W. DOEBLING, C. N. WOODS, A. KAUL, J. W. J. WALTER, AND M. L. ROGERS, *ExactPack Documentation*, tech. rep., Los Alamos National Laboratory, 2017.
- [38] T. SMITH, R. HOOPER, C. OBER, A. LORBER, AND J. SHADID, *Comparison of Operators for Newton-Krylov Method for Solving Compressible Flows on Unstructured Meshes*, in 42nd AIAA Aerospace Sciences Meeting and Exhibit, vol. 87, Reston, Virginia, 2004, American Institute of Aeronautics and Astronautics.
- [39] T. E. TEZDUYAR AND M. SENGA, *Stabilization and shock-capturing parameters in SUPG formulation of compressible flows*, Computer Methods in Applied Mechanics and Engineering, 195 (2006), pp. 1621–1632.
- [40] E. F. TORO, *Riemann Solvers and Numerical Methods for Fluid Dynamics*, 3rd ed., 2009.